Typeset using LaTeX in style in AASTeX62

# Search for gravitational waves from a long-lived remnant of the binary neutron star merger GW170817

THE LIGO SCIENTIFIC COLLABORATION AND THE VIRGO COLLABORATION

(Dated: 2019-04-11; report no. LIGO-P1800195)

## ABSTRACT

One unanswered question about the binary neutron star coalescence GW170817 is the nature of its post-merger remnant. A previous search for post-merger gravitational waves targeted high-frequency signals from a possible neutron star remnant with a maximum signal duration of 500 s. Here we revisit the neutron star remnant scenario with a focus on longer signal durations up until the end of the second Advanced LIGO-Virgo observing run, 8.5 days after the coalescence of GW170817. The main physical scenario for such emission is the power-law spindown of a massive magnetar-like remnant. We use four independent search algorithms with varying degrees of restrictiveness on the signal waveform and different ways of dealing with noise artefacts. In agreement with theoretical estimates, we find no significant signal candidates. Through simulated signals, we quantify that with the current detector sensitivity, nowhere in the studied parameter space are we sensitive to a signal from more than 1 Mpc away, compared to the actual distance of 40 Mpc. This study however serves as a prototype for post-merger analyses in future observing runs with expected higher sensitivity.

*Keywords:* gravitational waves – methods: data analysis – stars: neutron

## 1. INTRODUCTION

The binary neutron star (BNS) observation GW170817 (Abbott et al. 2017d) was the first multimessenger astronomy event jointly detected in gravitational waves (GWs) and at many electromagnetic (EM) wavelengths (Abbott et al. 2017e). It originated remarkably close to Earth, with a distance of $38^{+8}_{-18}$ Mpc[1] as measured by the LIGO and Virgo GW detectors (Aasi et al. 2015a; Acernese et al. 2015) alone and consistent EM distance estimates for the host galaxy NGC4993 (Sakai et al. 2000; Freedman et al. 2001; Hjorth et al. 2017; Lee et al. 2018).

A BNS merger is expected to leave behind a remnant compact object, either a light stellar-mass black hole or a heavy neutron star (NS), which can emit a variety of post-merger GW signals. These are more difficult to detect than the pre-merger inspiral signal, but the nearby origin of GW170817 has still generated interest in searching for a post-merger signal. Identifying the nature of the remnant would be highly valuable for improving, among other things, constraints on the nuclear equation of state (EoS) (Margalit & Metzger 2017; Bauswein et al. 2017; Rezzolla et al. 2018; Radice et al. 2018) over those obtained from the inspiral alone (e.g., Abbott et al. 2017d, 2018c, 2019).

Abbott et al. (2017g) presented a first model-agnostic search for short ($\lesssim 1$ s) and intermediate-duration ($\lesssim 500$ s) GW signals. No signal candidates were found. The search sensitivity was estimated for several GW emission mechanisms: oscillation modes of a short-lived hypermassive NS, bar-mode instabilities, and rapid spindown powered by magnetic-field induced ellipticities. For all mechanisms, a realistic signal from a NS remnant of GW170817 could only have been detected with at least an order of magnitude increase in detector strain sensitivity. A seconds-long postmerger signal candidate was reported by van Putten & Della Valle (2018) with an estimated GW energy lower than the sensitivity estimates of Abbott et al. (2017g).

An additional analysis in Abbott et al. (2019) used a Bayesian wavelet-based method to put upper limits on the energy and strain spectral densities over 1 s of data around the coalescence. These strain upper limits are 3–10 times above the numerical relativity expectations for post-merger emission from a hypermassive NS at 40 Mpc.

In this paper, we focus on a long-lived NS remnant, covering possible signal durations which at the long end are limited by the end of the second observing run (O2) on 2017-08-26, giving a total data set spanning 8.5 days from merger. The shortest signal durations we cover are $\sim$ hundreds of seconds after merger, so that the new search presented here

[1] Updated distance estimate corresponding to Fig. 3 of Abbott et al. (2019), where the sky location of the counterpart is not assumed, hence differing slightly from the one quoted in the text for fixed-location runs.

only partially overlaps with the intermediate-duration search from Abbott et al. (2017g). We assume the sky location of the EM counterpart (Coulter et al. 2017; Abbott et al. 2017e).

From considerations of realistic remnant NS properties, detailed in Sec. 2, we do not expect to make a detection with this search. Instead, the goal—as before in Abbott et al. (2017g)—is mainly to make sure that no unexpected signal is missed in the longer-duration part of the parameter space. This study also serves as a rehearsal for future post-merger searches with improved detectors. Hence, we use four search methods with varying restrictiveness on the signal shape and different ways of dealing with noise artefacts: two generic unmodeled algorithms and two that use templates based on a power-law spin-down waveform model.

The *Stochastic Transient Analysis Multidetector Pipeline* (STAMP, Thrane et al. 2011) is an unmodeled method using cross-power spectrograms. It was already used for the intermediate-duration analysis in Abbott et al. (2017g), but is employed here in a different configuration optimized for much longer signal lengths.

The other three algorithms are derived from methods originally developed to search for continuous waves (CWs): persistent, nearly-monochromatic GW signals from older NSs. (For reviews, see Prix 2009; Riles 2017.). Some CW searches have targeted relatively young NSs (Aasi et al. 2015b; Sun et al. 2016; Zhu et al. 2016), and adaptations of CW search methods to long-duration transient signals have been suggested before (Prix et al. 2011; Keitel 2016). However, the present search is the first time that any CW algorithms have been modified in practice (on real data) to deal with transients of rapid frequency evolution.

Specifically, these three are *Hidden Markov Model* (HMM) tracking (Suvorova et al. 2016; Sun et al. 2018)—a template-free algorithm previously used to search for CWs from the binary Scorpius X-1 (Abbott et al. 2017f)—and two new model-dependent methods—*Adaptive Transient Hough* (ATrHough, Oliver et al. 2019) and *Generalized FrequencyHough* (FreqHough, Miller et al. 2018)—based on algorithms (Krishnan et al. 2004; Sintes & Krishnan 2007; Aasi et al. 2014; Palomba et al. 2005; Antonucci et al. 2008; Astone et al. 2014) previously used in CW all-sky searches (e.g., most recently in Abbott et al. 2017a, 2018b).

After discussing the astrophysical motivation and context for this search in Sec. 2, presenting the analyzed data set in Sec. 3 and the four search methods in Sec. 4, we discuss the combined search results in Sec. 5 and conclude with remarks on future applications in Sec. 6. Additional results and details on the search methods are given in the appendices.

## 2. ASTROPHYSICAL BACKGROUND AND WAVEFORM MODEL

The probability for a long-lived NS remnant after a BNS merger depends on the progenitor properties and on the nuclear EoS (Baiotti & Rezzolla 2017; Piro et al. 2017). Using the progenitor masses and spins as measured from the inspiral (Abbott et al. 2017d, 2019), for many EoS the preferred scenarios are prompt collapse to a black hole or the formation of a hypermassive NS whose mass cannot be supported by uniform rotation and thus collapses in $\lesssim 1$ s (Abbott et al. 2017c). However, a supramassive NS—less massive, but above the maximum mass of a non-rotating NS and stable for up to $\sim 10^4$ s (Ravi & Lasky 2014)—or even a long-time stable NS could also be consistent with some physically-motivated EoS which allow for high maximum masses.

From the EM observational side, circumstantial evidence points towards a short-lived hypermassive NS (Kasen et al. 2017; Granot et al. 2017, 2018; Pooley et al. 2018; Matsumoto et al. 2018); though several authors (Yu et al. 2018; Ai et al. 2018; Geng et al. 2018; Li et al. 2018) consider continued energy injection from a long-lived remnant NS. Given this inconclusive observational situation, we agnostically consider the possibility of GW emission from a long-lived remnant NS and seek here to constrain it from the LIGO data.

In two of our search methods, and to estimate search sensitivities with simulations, we use a waveform model (Lasky et al. 2017; Sarin et al. 2018) originating from the general torque equation for the spindown of a rotating NS:

$$\dot{\Omega} = -k\,\Omega^n. \tag{1}$$

Here, $\Omega = 2\pi f$ and $\dot{\Omega}$ are the star's angular frequency and its time derivative, respectively, and $n$ is the braking index. A value of $n \leq 3$ corresponds to spindown predominantly through magnetic dipole radiation and $n = 5$ to pure GW emission (Shapiro & Teukolsky 1983). A braking index of $n = 7$ is conventionally associated with spindown through unstable $r$-modes (e.g., Owen et al. 1998), although the true value can be less for different saturation mechanisms (Alford & Schwenzer 2015, 2014). The value of $k$ also depends on these mechanisms; together with the starting frequency $\Omega_0$ it defines a spin-down timescale parameter

$$\tau = -\frac{\Omega_0^{1-n}}{k(1-n)}\,. \tag{2}$$

Integrating Eq. (1) and solving for the GW frequency gives the GW frequency evolution

$$f_{\rm gw}(t) = f_{\rm gw0}\left(1 + \frac{t}{\tau}\right)^{1/(1-n)}, \tag{3}$$

where $f_{\rm gw} = 2f$, $f_{\rm gw0}$ is the initial frequency at a starting time $t_{\rm start}$ (e.g., coalescence time $t_{\rm c}$ of the BNS merger), and $t$ is measured relative to $t_{\rm start}$.

The dimensionless GW strain amplitude for a non-axisymmetric rotating body following Eq. 3 is given by

$$h_0(t) = \frac{4\pi^2 G I_{zz}}{c^4}\frac{\epsilon}{d} f_{\rm gw0}^2 \left(1+\frac{t}{\tau}\right)^{2/(1-n)} . \quad (4)$$

Here, $I_{zz}$ is the principal moment of inertia, $\epsilon$ is the ellipticity of the rotating body, $d$ is the distance to the source, $G$ is the gravitational constant, and $c$ is the speed of light. This model assumes that $n$, $\epsilon$ and $I_{zz}$ are constant throughout the spin-down phase, while in reality the spindown could be e.g. GW-dominated at early times and then transition into EM dominance, and $I_{zz}$ can decrease with $\Omega$.

Our set of pipelines also allows for the power-law spin-down model to be valid for only part of the observation time: To accomodate the possibility that the newborn NS has not immediately settled into a state that obeys the power-law model, the FreqHough analysis starts a few hours after the merger (at $t_{\rm c} \approx 1187008882.443$ in GPS seconds, with the offset $\Delta t$ varying across parameter space as described later), making no assumption about the earlier NS evolution. This provides complementary constraints to the other analyses. The unmodeled STAMP search is also sensitive to signals starting at either $t_{\rm c}$ or at any later time, as it does not impose a fixed starting time for any time-frequency tracks. Moreover, neither STAMP nor HMM impose the specific waveform model for their initial candidate selection.

The theoretical detectability of newborn NSs evolving according to the spin-down model, Eq. (3), has been explored previously, beginning with simple matched-filter estimates (Palomba 2001; Dall'Osso et al. 2009). More recent estimates also consider the limitations of practical searches in the context of magnetars born following core-collapse supernovae (Dall'Osso et al. 2018) and long-lived post-merger remnants (Dall'Osso et al. 2015, 2018; Sarin et al. 2018), finding qualitatively similar results. With Advanced LIGO (aLIGO) at design sensitivity (Abbott et al. 2018d) and an optimal matched-filter analysis, at $d = 40$ Mpc an ellipticity $\epsilon \sim 10^{-2}$ and timescale $\tau \gtrsim 10^4$ s would be required. However, such large $\epsilon$ and long $\tau$ would imply more energy emitted than is available from the remnant's initial rotation. Considering actual data analysis pipelines applied to real detector data (at O2 sensitivity), a detectable signal only seems possible for extremely large $\epsilon \geq 0.1$ and short $\tau$ due to the energy budget constraint (Sarin et al. 2018). Such ellipticities are physically unlikely (Johnson-McDaniel & Owen 2013) and would require internal magnetic fields greater than $\sim 10^{17}$ G (e.g., Cutler 2002), which might be intrinsically unstable (Reisenegger 2009) and for which very rapid EM-dominated spindown would be expected.

For r-modes, the GW strain follows a different relation than Eq. 4 (Owen et al. 1998), but the physically relevant parameter (the saturation amplitude) is also expected to be small (Arras et al. 2003; Bondarescu et al. 2009). They could be an important emission channel especially at high frequencies, and the search presented in this paper also covers braking indices up to $n = 7$. The sensitivity estimates presented in Sec. 5 however, for simplicity, will be for $n = 5$ only.

Still, with this first search for long-duration post-merger signals, we demonstrate that available analysis methods can comprehensively cover the relevant parameter space, and thus will be ready once detector sensitivity has improved, or in the case of a fortunate, very nearby BNS event.

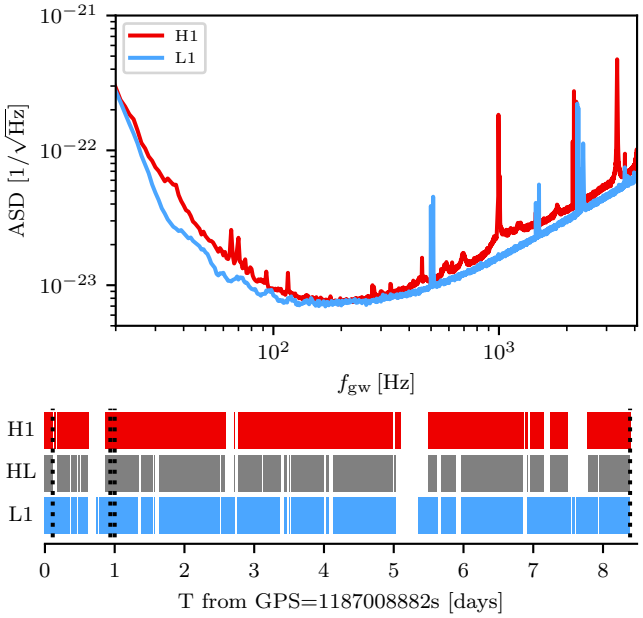


**Fig1.** Top panel: Noise strain amplitude spectral density (ASD) curves of LIGO Hanford (H1) and Livingston (L1) on August 17, 2018. (Averaged over 1800 s stretches including GW170817.) Lower panel: Analysable science mode data segments for the remaining O2 run after the GW170817 event. Vertical dotted lines mark the analysis end times, from left to right, for HMM, FreqHough, ATrHough and STAMP.

## 3. DETECTORS AND DATA SET

In this analysis, we use data from the two aLIGO detectors in Hanford, Washington (H1) and Livingston, Louisiana (L1). No data from Virgo (Acernese et al. 2015) or GEO600 (Dooley et al. 2016) was used because of their lower sensitivity.[2] Three of the pipelines use data up to 2 kHz; STAMP also uses data up to 4 kHz. Both detectors in their O2 configuration had their best sensitivity in the 100–200 Hz range, with significantly less sensitivity in the kHz range (e.g. a factor ∼4 worse in strain at 2 kHz)—see Fig. 1. For the lower analysis cutoff of each pipeline, see Sec. 4.

[2] E.g. at 500 Hz the noise strain amplitude spectral density was about a factor of $\sim 5$ for Virgo and $\sim 20$ for GEO600 worse than for L1 in late O2.

Starting from a rounded GW170817 coalescence time of $t_c \approx 1187008882$ s, the HMM pipeline uses 9688 s of data (until the first gap in H1 data), ATrHough uses 1 day of data after $t_c$, FreqHough analyzes from 1 to about 18 hours after $t_c$ in different configurations, and STAMP analyzes the whole 8.5 days of data until the end of O2 on 2017-08-26. The duty cycle of both detectors (H1, L1) was 100% during the first 9688 s after the merger, (70%, 78%) for the first day (62% in coincidence), and (83%, 85%) for the full data set (75% in coincidence). The analysed data segments are also illustrated in Fig. 1. STAMP processes the $h(t)$ strain data into cross-power time-frequency maps (see Sec. 4.1 for details), while for the other pipelines the basic analysis units are Short Fourier Transforms (SFTs) of 1–8 s duration.

Several known noise sources have been subtracted from the strain data using a new automated procedure (Davis et al. 2019) applied to the full O2 data set, processing a much larger amount of time than the cleaning method (Driggers et al. 2019) used for the shorter data sets analysed in previous GW170817 publications. Calibration uncertainties (Cahillane et al. 2017) for this data set are estimated as below 4.3% in amplitude and 2.3 degrees in phase for 20–2000 Hz, and 4.5% in amplitude and 3.8 degrees in phase for 2–4 kHz; these are tighter than for the initial calibration version used in Abbott et al. (2017g). These uncertainties are not explicitly propagated into the sensitivity estimates presented in this paper, since they are smaller than other uncertainty contributions and the degeneracies in amplitude parameters.

## 4. SEARCH METHODS AND CONFIGURATIONS

Here we briefly describe the four search methods, first the unmodeled STAMP and HMM pipelines and then the two Hough pipelines tailored to the power-law spindown model. Additional details can be found in Appendix A.

Each analysis uses the known sky location of the counterpart near RA = 13.1634 hrs, Dec. = $-23.3815°$ (Coulter et al. 2017; Abbott et al. 2017e), but makes different choices for the analysed data span. The recovery efficiency of each algorithm is studied with simulated signals under the waveform model from Sec. 2, as described in Sec. 5 and Appendix B.

A summary of configurations for all four pipelines, both for the main search and the sensitivity estimation simulations, is given in Table 1.

### 4.1. *STAMP*

STAMP (Thrane et al. 2011) is an unmodeled search pipeline designed to detect gravitational wave transients. Its basic unit is a spectrogram made from cross-correlated data between two detectors. Narrowband transient gravitational waves produce tracks of excess power within these spectrograms, and can be detected by pattern recognition algorithms. Each spectrogram pixel is normalized with the noise to obtain a signal-to-noise ratio (SNR) for each pixel.

STAMP was used in the first GW170817 post-merger search (Abbott et al. 2017g) in a configuration with 500 s long spectrograms. To increase sensitivity to longer GW signals, here we use spectrogram maps of 15 000 s length. The search is split into two frequency bands from 30–2000 Hz and 2000–4000 Hz. The former uses pixels of $100\,\mathrm{s} \times 1\,\mathrm{Hz}$, while the latter uses shorter-duration pixels of $50\,\mathrm{s} \times 1\,\mathrm{Hz}$ to limit SNR loss due to the Earth's rotation changing the phase difference between detectors.

We then use Stochtrack (Thrane & Coughlin 2013), a seedless clustering algorithm, to identify significant clusters of pixels within these maps. The algorithm uses one million quadratic Bézier curves as templates for each map, and the loudest cluster is picked for each map. More details about the pixel size choice, the detection statistic and the search results are in Appendix A.1.

The on-source data window is from just after the time of the merger to the end of O2 (1187008942–1187733618). To measure the background and estimate the significance of the clusters found, we run the algorithm on time-shifted data from June 24th to just before the merger.

### 4.2. *HMM tracking*

Hidden Markov model (HMM) tracking provides a computationally efficient strategy for detecting and estimating a quasimonochromatic GW signal with unknown frequency evolution and stochastic timing noise (Suvorova et al. 2016; Sun et al. 2018). It was applied to data from the first aLIGO observing run to search for CWs from the low-mass X-ray binary Scorpius X-1 (Abbott et al. 2017f). The revision of the algorithm in Sun et al. (2018) is also well suited to searching for a long-transient signal from a BNS merger remnant, if the spin-down time-scale is in the range $10^2\,\mathrm{s} \lesssim \tau \lesssim 10^4\,\mathrm{s}$.

A HMM is an automaton based on a Markov chain (a stochastic process transitioning between discrete states at discrete times), composed of a hidden (unmeasurable) state variable and a measurement variable. A HMM is memoryless, i.e., the hidden state at time $t_{n+1}$ only depends on the state at time $t_n$, with a certain transition probability. The most probable sequence of hidden states given the observations is computed by the classic Viterbi algorithm (Viterbi 1967). Details on the probabilistic model can be found in Appendix A.2.

In this analysis, we track the GW signal frequency as the hidden variable, with its discrete states mapped one-to-one to the frequency bins in the output of a frequency-domain estimator computed over an interval of length $T_{\mathrm{drift}}$. We aim at searching for signals with $10^2\,\mathrm{s} \lesssim \tau \lesssim 10^4\,\mathrm{s}$, such that the first time derivative $\dot{f}_{\mathrm{gw}}$ of the signal frequency $f_{\mathrm{gw}}$ satisfies $\dot{f}_{\mathrm{gw}} \approx f_{\mathrm{gw}}/\tau \lesssim 1\,\mathrm{Hz\,s^{-1}}$, given $T_{\mathrm{drift}} = 1\,\mathrm{s}$ and a frequency bin width of $\Delta f = 1\,\mathrm{Hz}$. The motion of the Earth with respect to the solar system barycenter (SSB) can be neglected during a $T_{\mathrm{drift}}$ interval. Hence we use a running-mean nor-

**H.** Configurations of the four analysis pipelines used in this paper.

| | STAMP | HMM | ATrHough | FreqHough |
|---|---|---|---|---|
| search start[a] | $t_c$ | $t_c$ | $t_c$ | $t_c$+ (1–7) hours[b] |
| search duration [hours] | 201.3[c] | 2.7 | 24 | 2–18[b] |
| $f_{gw}$ data range [Hz] | 30–4000[c] | 100–2000 | 187–2000 | 50–2000 |
| $n$ coverage | *unmodeled* | *unmodeled* | 2.5–7.0 | 2.5–7.0 |
| $f_{start}$ coverage [Hz][d] | *unmodeled* | *unmodeled* | 500–2000 | 500–2000 |
| $\tau$ coverage [s] | *unmodeled* | *unmodeled* | $10^2$–$10^5$ | 10–$10^5$ |
| *injection set for sensitivity estimation*[e] | | | | |
| signal start[a] | random | $t_c$ | $t_c$ | $t_c$+ [1,2,5] hours[b] |
| $n$ coverage | 5.0 | 2.5–7.0 | 5.0 | 5.0 |
| $f_{start}$ coverage [Hz][d] | 500–3000 | 500–2000 | 550–2000 | 390–2000 |
| $\tau$ coverage [s] | $10^2$–$10^4$ | $10^2$–$10^4$ | $6\times10^2$–$3\times10^4$ | $4\times10^2$–$2\times10^4$ |
| inclination $\cos\iota$ | 0.0, 1.0 | random | 0.0, 1.0 | random |

[a] Coalescence time $t_c \approx 1187008882$ rounded to integer GPS seconds.

[b] FreqHough search start and duration vary across parameter space.

[c] In separate maps of 15 000 s length and 20–2000 Hz and 2000–4000 Hz configurations.

[d] $f_{start} = f_{gw}(t=0)$ for HMM and ATrHough; $f_{start} = f_{gw}(t=\Delta t)$ for STAMP and FreqHough.

[e] Discrete sets of injections within these ranges; not all combinations used. See Sec. 5 and the per-pipeline tables in the appendix for details.

malized power in SFTs with length $T_{SFT} = T_{drift} = 1$ s as the estimator to calculate the HMM emission probability.

We analyze 9688 s of data (GPS times 1187008882–1187018570) in a 100–2000 Hz frequency band with multiple configurations optimized for different $\tau$. We do not analyze longer data stretches because (i) several intervals in the data after GPS time 1187018570 are not in analysable science mode, and (ii) signals with $10^2\,\mathrm{s} \lesssim \tau \lesssim 10^4\,\mathrm{s}$ drop below the algorithm's sensitivity limit after $\sim 10^4$ s; observing longer merely accumulates noise without improving SNR. The 9688 SFTs are Hann-windowed. The detection statistic $\mathcal{P}$ is defined in Eqn. A11. The methodology and analysis is fully described in Sun & Melatos (2018).

### 4.3. *Adaptive Transient Hough*

The Adaptive Transient Hough search method is described in detail in Oliver et al. (2019). It follows a semi-coherent strategy similar to the SkyHough (Krishnan et al. 2004; Sintes & Krishnan 2007; Aasi et al. 2014) all-sky CW searches, but adapted to rapid-spindown transient signals.

We start from data in the form of Hann-windowed SFTs with lengths of [1,2,4,6,8] s, covering one day after merger (GPS times 1187008882–1187095282). These are digitized by setting a threshold of 1.6 on their normalized power, as first derived by Krishnan et al. (2004), replacing each SFT by a collection of zeros and ones called a peak-gram. For each point in parameter space, the Hough number count is the weighted sum of the peak-grams across a template track accounting for Doppler shift and the spindown of the source. The use of weights minimizes the influence of time-varying detector antenna patterns and noise levels (Sintes & Krishnan 2007). For this post-merger search it also accounts for the amplitude modulation related to the transient nature of the signal.

The search parameter space for the model from Sec. 2 covers a band of 500–2000 Hz in starting frequencies $f_{gw0}$, braking indices of $2.5 \le n \le 7$ and spindown timescales of $10^2 \le \tau \le 10^5$ s. The search runs over 16042 subgroups, each containing a range of 150 Hz in $f_0$, 0.25 in $n$ and 1000 s in $\tau$. Each subgroup is analyzed with the longest possible SFTs according to the criterion (Oliver et al. 2019)

$$T_{SFT} \le \frac{\sqrt{(n-1)\tau}}{\sqrt{f_{gw}}}\,, \tag{5}$$

and for each template the observation time is selected as $T_{obs} = \min(4\,\tau, 24\,\mathrm{hours})$. Over the whole template bank, the search uses data from 187–2000 Hz.

Each template is ranked based on the deviation of its weighted number count from the theoretical expectation for Gaussian noise (the critical ratio) as described in appendix A.3. The detection threshold corresponds to a two-detector $5\sigma$ false alarm probability for the entire template bank. A per-detector critical ratio threshold was also set to check the consistency of a signal between H1 and L1.

### 4.4. *Generalized FrequencyHough*

The FrequencyHough is a pattern-recognition technique originally developed to search for CWs by mapping points in time-frequency space of the detector to lines in frequency-spindown space (Antonucci et al. 2008; Astone et al. 2014). This only works if the signal frequency varies in time very slowly. Miller et al. (2018) have generalized the FrequencyHough for postmerger signals, where we expect much higher spindowns.

The search starts at a time offset $\Delta t = t_{\rm start} - t_{\rm c}$ after coalescence time $t_{\rm c}$, so that the waveform model is interpreted with starting frequency $f_{\rm start} = f_{\rm gw}(t = \Delta t)$ taking the place of $f_{\rm gw0}$ in Eq. 3. In this way, assuming that the NS has already spun down before $t_{\rm start}$ following some arbitrary track, we would be probing higher initial frequencies and spindowns through a less challenging parameter space during the search window. Furthermore, the source parameters $(n, f_{\rm start}, \tau)$ are transformed to new coordinates such that in the new space the behavior of the signal is linear. See appendix A.4 for the transformation relations.

We search across the parameter space with a fine, nonuniform grid: For each braking index $n$, we do a Hough transform and then record the most significant candidates over the parameter range of the resulting map. This is done separately on the data from each detector, and then we check candidates for coincidence between detectors according to their Euclidean distance in parameter space.

The search is run in three configurations using varying $T_{\rm SFT} = 2, 4, 8\,$s, covering different observing times, starting $\Delta t$ = 1–7 hours after merger. It covers $n = [2.5, 7]$, $f_{\rm start} = [500, 2000]\,$Hz and $\tau = [10, 10^5]\,$s, analyzing detector data from 50 to 2000 Hz.

Candidates are also ranked by critical ratio (deviation from the theoretical expectation for Gaussian noise) in this analysis. Most can be vetoed by the coincidence step or by considering detector noise properties; a follow-up procedure for surviving candidates is also described in appendix A.4.

## 5. SEARCH RESULTS AND SENSITIVITY ESTIMATES

### 5.1. *Absence of significant candidates*

The four search methods all either found no significant candidates in the aLIGO data after GW170817; or those that were found, were clearly vetoed as instrumental artifacts.

For the unmodeled STAMP search, the loudest triggers in the low- and high-frequency bands have SNRs of 3.18 and 3.07 respectively. The time-shifted backgrounds only just start to drop off near these SNRs, so that they correspond to false-alarm probabilities $p_{\rm FA}$ of 0.81 and 0.80 which are completely consistent with noise. For reference, $p_{\rm FA} = 0.05$ would have only been reached for SNRs of $\gtrsim 4.9$ and $\gtrsim 3.5$ for these low- and high-frequency background distributions, respectively. (See Fig. 4 in appendix A.1.)

For HMM, the loudest trigger has a detection statistic $\mathcal{P} = 2.6749$ (as defined in Eq. A11), corresponding to a false-alarm probability of 0.01, right below the threshold set beforehand as significant enough for further study. The trigger is found with observing time $T_{\rm obs} = 200\,$s starting from $t = t_{\rm c}$. Monte-Carlo simulations show that for signals that this setup is sensitive to, higher $\mathcal{P}$ should be obtained with longer $T_{\rm obs}$. Follow-up analysis of the trigger with $300\,{\rm s} \leq T_{\rm obs} \leq 1000\,{\rm s}$ confirms that it does not follow this expectation; hence it is discarded as spurious.

ATrHough found 51 initial candidates over the covered part of $(n, f_{\rm gw0}, \tau)$ parameter space. All of these were excluded with the follow-up procedure described in appendix A.3 as inconsistent with the expected spindown model and more likely to be caused by monochromatic detector artifacts (lines) contaminating the search templates.

The FreqHough search returned 521 candidates over the covered part of $(n, f_{\rm start}, \tau)$ parameter space. We vetoed 10 of them because they were within frequency bands contaminated with known noise lines (Covas et al. 2018). 510 of the remaining candidates had much higher ($> 4$ times) critical ratios in H1 than in L1, which is inconsistent with true astrophysical signals when considering the relative sensitivities, duty factors and antenna patterns. There was one remaining candidate, with a critical ratio of 5.21 in H1 and 4.88 in L1, which was followed up and excluded with the procedure described in appendix A.4.

### 5.2. *Sensitivity estimates with simulated signals*

Starting from this non-detection result, we use simulated signals according to Eq. 3 to quantify the sensitivity of each analysis given the data set around the time of GW170817 and its known sky location. The sets of injected parameters are different for each pipeline, and there are also some differences in procedure: STAMP performs injections on the same data as the main search but with a non-physical time shift between the detectors (as in Abbott et al. 2017g, 2018a); HMM injects signals into the original set of SFTs but with randomly permuted timestamps; and the other two pipelines inject signals into exactly the same data as analysed in the main search. HMM and ATrHough perform all injections starting at merger time $t_{\rm c}$, with $f_{\rm gw0}$ in Eq. 3 interpreted as the frequency at $t_{\rm c}$, while injections for FreqHough are done at $\Delta t = 1, 2$ or 5 hours after $t_{\rm c}$, chosen as representative starting times for each search configuration, and $f_{\rm gw0}$ correspondingly set at $t_{\rm c} + \Delta t$. Similarly, STAMP treats $f_{\rm gw0}$ as the starting frequency of each injection, which have $\Delta t$ distributed through the whole search range, yielding a time-averaged sensitivity. In the following, we use $f_{\rm start}$ to refer to any of these choices.

These differences in injection procedure, and different choices of detection threshold, mean that any comparison of

the following results does not correspond to a representative evaluation of general pipeline performance, but is solely in the interest of estimating how much sensitivity is missing for a GW170817-like post-merger detection based on the specific configurations as used in the present search.

We focus here on results for a braking index of $n = 5$, as expected for spin-down dominated by GW emission from a static quadrupole deformation. The signal amplitude $h_0$ (as given in Eq. 4) is degenerate between the ellipticity $\epsilon$, moment of inertia $I_{zz}$ and distance $d$. We choose a fiducial value of $I_{zz} = 100\,M_\odot^3\,G^2/c^4 \approx 4.34 \times 10^{38}\,\mathrm{kg\,m^2}$, consistent with EoS yielding a supramassive or stable remnant: The high mass and assumed rapid rotation can increase the moment of inertia by more than a factor of 3 compared to a nonrotating NS of $1.4\,M_\odot$. In addition, EoS compatible with the high remnant mass favor larger moments of inertia already at lower mass. For a given set of model parameters $\{n = 5, f_{\mathrm{start}}, \tau\}$ we consider the maximum $\epsilon$ allowed by the initial rotational energy budget (Sarin et al. 2018): the total emitted GW energy as $t \to \infty$,

$$E_{\mathrm{gw}} = -\int_{t=t_{\mathrm{start}}}^{\infty} \mathrm{d}t\, \frac{32G}{5c^5}\, I_{zz}^2\, \epsilon^2\, \Omega^6(t)\,, \tag{6}$$

must not exceed the remnant's initial rotational energy $E_{\mathrm{rot}} = 0.5\, I_{zz}\, f_{\mathrm{start}}^2\, \pi^2$.

Given each pipeline's detection threshold, we can rescale the amplitude of simulated signals until 90% of them are recovered above threshold, while randomising over nuisance parameters (polarization angle and initial phase of the signal; also source inclination $\iota$ and signal start time for some of the pipelines). We can then either interpret this amplitude scaling as a need to lower the distance of simulated sources, i.e. estimating the sensitive distance $d^{90\%}$ of the search. Or we can fix the true distance to the source of GW170817 to obtain an energy upper limit $E_{\mathrm{gw}}^{90\%}$: For a remnant NS with the given parameters, we interpret the square of the amplitude scaling as the factor by which the energy output needs to be greater than the expected amount in order to produce signals that we can recover at 90% confidence. Both interpretations are shown in Fig. 2, with coverage of the injection sets illustrated in Fig. 3. Full results are listed in the Appendix in Tables 2–5.

The highest sensitivities are achieved at low $f_{\mathrm{start}}$ and for rapid spindown (low $\tau$). This is mostly due to the energy budget constraint enforced on $\epsilon$: In principle, higher $f_{\mathrm{start}}$ yield higher initial amplitudes and longer $\tau$ allow accumulation of SNR over longer observation times ($\mathrm{SNR} \propto \tau^{1/2}$ for $n = 5$ and once $T_{\mathrm{obs}} > \tau$). However, due to the energy budget constraint $\epsilon$ must be lower in this region of parameter space and hence actual detectability is reduced ($\mathrm{SNR} \propto \epsilon \propto \tau^{-1} f_{\mathrm{start}}^{-6}$).

The four pipelines perform differently across $\tau$ regimes: The unmodeled STAMP and HMM are most sensitive at the shortest $\tau = 10^2$ s, but lose up to an order of magnitude in $d^{90\%}$ when going to $\tau = 10^4$ s. On the other hand, the model-based semi-coherent ATrHough and FreqHough have focused on longer $\tau$ of $4 \times 10^2$ s to $3 \times 10^4$ s, with only up to a factor of 2 loss in $d^{90\%}$ for the longest $\tau$ at fixed $f_{\mathrm{start}}$. See Figs. 6–9 in the Appendix for sensitivity estimates over each pipeline's full injection set.

As this parameter dependence is shaped by the $E_{\mathrm{gw}} = E_{\mathrm{rot}}$ constraint, and also influenced by some practical tradeoffs in pipeline configuration, in this paper we do not attempt to provide a general evaluation of pipeline performance on fully equivalent injection sets, nor for generic GW signals. Such a comparison would require a detailed mock data challenge similar to Messenger et al. (2015) and Walsh et al. (2016). Instead, Fig. 2 shows results from each pipeline for the parts of parameter space where it achieved its highest sensitivity.

In summary, in no part of the $n = 5$ parameter space covered by the four search ranges and injection sets do we reach 90% sensitive distances of 1 Mpc or further. This corresponds to a lowest 90% detectable energy of $E_{\mathrm{gw}} \lesssim 8\,M_\odot c^2$ at $f_{\mathrm{start}} = 500$ Hz and $\tau = 100$ s. At higher $f_{\mathrm{start}}$, the sensitive distances for any $\tau$ are even lower due to the energy constraint. Note again that this covers power-law spindown signals both starting right at coalescence time $t_{\mathrm{c}}$ and signals starting with some time delay, with a delay time of 1–7 hours for FreqHough and any possible delay time until the end of O2 for STAMP.

At the shortest $\tau$, the parameter space covered here overlaps with the magnetar injections in the shorter-duration search of Abbott et al. (2017g)[3], though results in that paper were quoted as recoverable at 50% confidence, and hence are more optimistic than the new results at 90%. For example, at $f_{\mathrm{start}} = 1000$ Hz and $\tau = 100$ s, the STAMP analysis in the previous paper found $E_{\mathrm{gw}}^{50\%} \approx 24\,M_\odot c^2$ while the new STAMP and HMM analyses presented here obtain $E_{\mathrm{gw}}^{90\%} \approx 100\,M_\odot c^2$ at these parameters. For the pipelines in this paper, amplitudes for detectability at 50% confidence are typically lower by a factor of 2–4 than those at 90% confidence. While such lower thresholds would push the best $d^{50\%}$ limits up to a few Mpc, this would not change the conclusion that any GWs from a long-lived remnant of GW170817 at 40 Mpc would be undetectable.

## 6. CONCLUSION

[3] We note here a mistake in Abbott et al. (2017g): In section 3.2.4, the equivalent energies for the best STAMP results should have read $E_{\mathrm{gw}} \approx 0.6 M_\odot c^2$ for bar modes and $E_{\mathrm{gw}} \approx 10 M_\odot c^2$ for the magnetar model, instead of the quoted 2 and 4 $M_\odot c^2$. The corresponding $h_{\mathrm{rss}}$ values in the text of Abbott et al. (2017g) and in its Tables 2 and 3, as well as Figure 1, are correct as published.

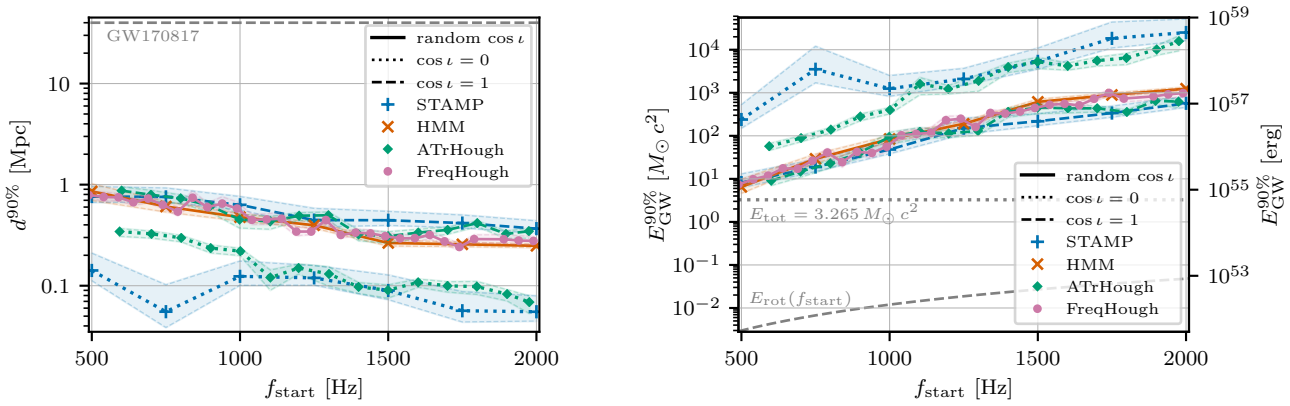


**Fig 2.** A sample of search sensitivities achieved for the power-law spindown signal model with braking index $n = 5$. Results are shown as sensitive distance $d^{90\%}$ (left panel) for otherwise physical parameters, or as required emitted energy $E_{\rm gw}^{90\%}$ at a fixed distance $d = 40$ Mpc (right panel), both as a function of reference starting frequency $f_{\rm start}$ used for the injections of each pipeline. ($f_{\rm start} = f_{\rm gw}(t = \Delta t)$ for STAMP and FreqHough and $f_{\rm start} = f_{\rm gw0} = f_{\rm gw}(t = 0)$ for the others.)
See Fig. 3 for the parameter ranges covered by each injection set. This figure shows the subset with highest sensitivity for each analysis; this corresponds to the shortest ($\tau = 100$ s) injections for STAMP and HMM, while for ATrHough and FreqHough $\tau(f_{\rm start})$ is variable, depending on the search coherence length, as also listed in Tables 4 and 5. Note that detection thresholds are also different between pipelines.
The NS ellipticity $\epsilon$ is always chosen as the maximum allowed by the energy budget constraint $E_{\rm gw} = E_{\rm rot}$ at each $(n, f_{\rm start}, \tau)$ parameter point, assuming a NS moment of inertia of $I_{zz} = 100\, M_\odot^3\, G^2/c^4 \approx 4.34 \times 10^{38}\,\mathrm{kg\,m^2}$. Injections were randomized over source inclination $\cos\iota$ for HMM and FreqHough, while for STAMP and ATrHough injections for the best case ($\cos\iota = 1$) and worst case ($\cos\iota = 0$) are shown separately.
For comparison, the known distance to the source of GW170817 is indicated by a horizontal dashed line in the left panel, as well as two (optimistic) energy upper limits in the right panel: the total system energy (dotted line, using a fiducial value of $E_{\rm tot} = 3.265 M_\odot c^2$ as in Abbott et al. 2017g) and the initial rotational energy $E_{\rm rot}$ as a function of $f_{\rm start}$ (dashed line).

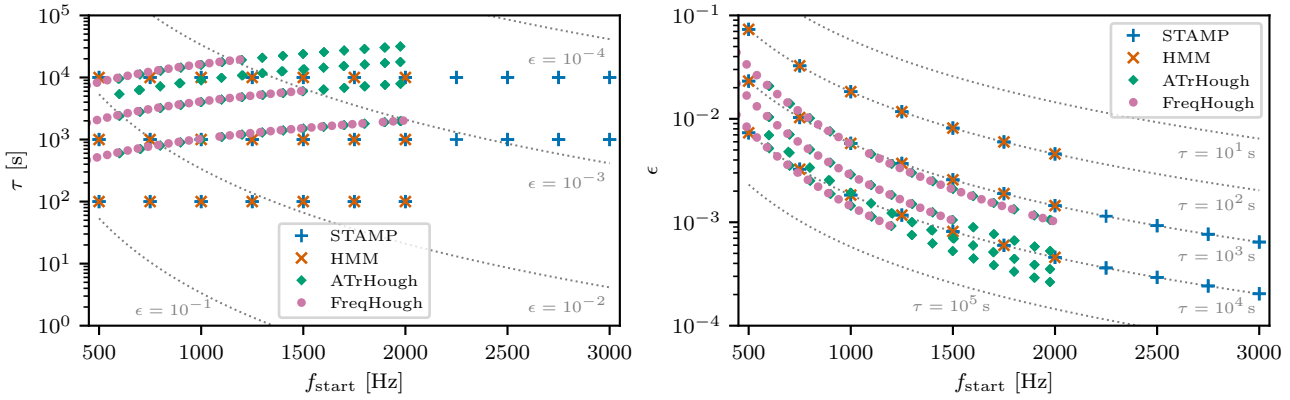


**Fig 3.** Parameter coverage in $f_{\rm start}$, $\tau$ and $\epsilon$ of the injection sets used for the $n = 5$ sensitivity estimates, as listed in Tables 2–5. As shown in the left panel, the HMM and STAMP injections are at fixed $\tau \in [10^2, 10^3, 10^4]$ s, while for ATrHough and FreqHough different $\tau(f_{\rm start})$ curves are covered for different choices of $T_{\rm SFT}$ (and, in the case of FreqHough, $\Delta t$) in the search setup. At each $(n, f_{\rm start}, \tau)$ parameter space point, the maximum $\epsilon$ allowed by the energy budget ($E_{\rm gw} = E_{\rm rot}$) is chosen (right panel), assuming a NS moment of inertia of $I_{zz} = 100\, M_\odot^3\, G^2/c^4 \approx 4.34 \times 10^{38}\,\mathrm{kg\,m^2}$. Lines of constant $\epsilon$ (left panel) or $\tau$ (right panel) are shown for comparison. STAMP injections include $f_{\rm start}$ up to 3000 Hz for longer $\tau$, with those above 2000 Hz covered by the high-frequency search configuration. But for $\tau = 100$ s, we limit $f_{\rm start}$ to 2000 Hz because injections at higher frequencies would leave the high-frequency band too rapidly to be recoverable.

We have searched for GW emission from a putative remnant neutron star of the BNS merger GW170817, concentrating on signals lasting from hundreds of seconds upwards and described by a power-law spin-down model. Two of the four employed analysis methods however were designed to be sensitive to any generic signal morphology in the covered observation time. In keeping with the available energy budget and theoretical sensitivity estimates, we have not found any significant signal candidates. Studies with simulated signals confirm that we would have only been sensitive to a signal from GW-dominated spin-down (at the time and sky location of GW170817) for distances of less than 1 Mpc, or equivalently for unphysical amounts of emitted GW energy.

The four analysis pipelines used in this work have complementary strengths in parameter space coverage and in their response to noise artifacts and gaps in the data. While further development of these methods is expected, improvements are also needed—and already in progress—on the instrumentation side. Ongoing instrumental enhancements of Advanced LIGO and Virgo towards their design sensitivies (Abbott et al. 2018d), and further upgrades like LIGO A+ (Barsotti et al. 2018) in the next decade, will improve strain sensitivity across the detector band. Improved high-frequency performance is of particular importance for post-merger searches, as the highest signal amplitudes are emitted in the early, high-frequency part of the spin-down, where the detectors are currently much less sensitive than around a few hundred Hz. Searches for long-duration post-merger signals from supramassive or stable NSs could then enter into the astrophysically constraining regime. However, from scaling the sensitivies obtained in this analysis (or even those estimated for an optimal matched-filter analysis by Sarin et al. 2018) with the expected improvements of 2–4 in strain, they will still be limited to the most nearby BNS events.

Third generation detectors, such as the Einstein Telescope (Hild et al. 2011; Sathyaprakash et al. 2012) and Cosmic Explorer (Abbott et al. 2017b), promise a strain sensitivity increase of $\sim$ 20–30 over aLIGO at design sensitivity. GWs from a long-lived remnant of another BNS at the same distance as GW170817 should then become observable.

The authors gratefully acknowledge the support of the United States National Science Foundation (NSF) for the construction and operation of the LIGO Laboratory and Advanced LIGO as well as the Science and Technology Facilities Council (STFC) of the United Kingdom, the Max-Planck-Society (MPS), and the State of Niedersachsen/Germany for support of the construction of Advanced LIGO and construction and operation of the GEO600 detector. Additional support for Advanced LIGO was provided by the Australian Research Council. The authors gratefully acknowledge the Italian Istituto Nazionale di Fisica Nucleare (INFN), the French Centre National de la Recherche Scientifique (CNRS) and the Foundation for Fundamental Research on Matter supported by the Netherlands Organisation for Scientific Research, for the construction and operation of the Virgo detector and the creation and support of the EGO consortium. The authors also gratefully acknowledge research support from these agencies as well as by the Council of Scientific and Industrial Research of India, the Department of Science and Technology, India, the Science & Engineering Research Board (SERB), India, the Ministry of Human Resource Development, India, the Spanish Agencia Estatal de Investigación, the Vicepresidència i Conselleria d'Innovació, Recerca i Turisme and the Conselleria d'Educació i Universitat del Govern de les Illes Balears, the Conselleria d'Educació, Investigació, Cultura i Esport de la Generalitat Valenciana, the National Science Centre of Poland, the Swiss National Science Foundation (SNSF), the Russian Foundation for Basic Research, the Russian Science Foundation, the European Commission, the European Regional Development Funds (ERDF), the Royal Society, the Scottish Funding Council, the Scottish Universities Physics Alliance, the Hungarian Scientific Research Fund (OTKA), the Lyon Institute of Origins (LIO), the Paris Île-de-France Region, the National Research, Development and Innovation Office Hungary (NKFI), the National Research Foundation of Korea, Industry Canada and the Province of Ontario through the Ministry of Economic Development and Innovation, the Natural Science and Engineering Research Council Canada, the Canadian Institute for Advanced Research, the Brazilian Ministry of Science, Technology, Innovations, and Communications, the International Center for Theoretical Physics South American Institute for Fundamental Research (ICTP-SAIFR), the Research Grants Council of Hong Kong, the National Natural Science Foundation of China (NSFC), the Leverhulme Trust, the Research Corporation, the Ministry of Science and Technology (MOST), Taiwan and the Kavli Foundation. The authors gratefully acknowledge the support of the NSF, STFC, MPS, INFN, CNRS and the State of Niedersachsen/Germany for provision of computational resources. This article has been assigned document number LIGO-P1800195.

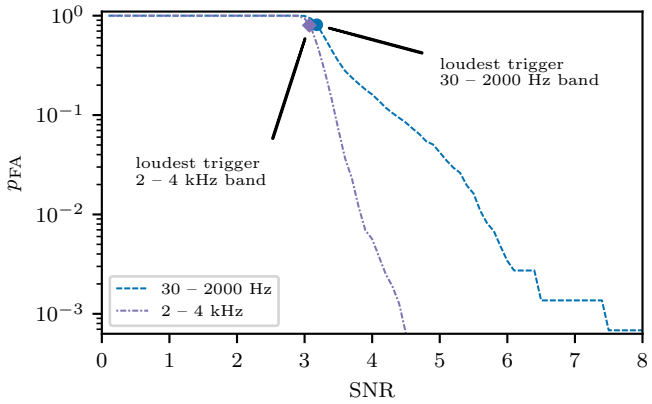


**Fig 4.** STAMP background distributions, (in terms of false alarm probability $p_{\rm FA}$ as a function of detection statistic (SNR), for the low- and high-frequency bands, and the corresponding loudest foreground triggers (dot and diamond symbols).

# APPENDIX

## A. ADDITIONAL DETAILS ON SEARCH METHODS

### A.1. *STAMP*

*Spectrogram pixel sizes*—The low frequency band from 30–2000 Hz uses pixels of $100\,\mathrm{s} \times 1\,\mathrm{Hz}$, while the high frequency band from 2000–4000 Hz uses pixels of smaller durations of $50\,\mathrm{s} \times 1\,\mathrm{Hz}$. Smaller pixels at higher frequency are necessary to account for the rotation of the Earth, which causes the GW phase difference between detectors to change with time. If the pixel durations are too large, this results in a loss of SNR which increases with frequency. The durations are thus chosen to limit the maximum possible SNR loss in a pixel (at the highest frequencies) from this effect to about $10\%$ (Thrane et al. 2015).

*Detection statistic*—Each spectrogram in the STAMP search (Thrane et al. 2011; Thrane & Coughlin 2013; Thrane et al. 2015) is analyzed with many randomly chosen quadratic Bézier curves. The SNR of each track $\rho_\Gamma$ is a weighted sum of the SNR of the pixels covered by the track. The quantity $\rho_\Gamma$ also serves as the detection statistic and is calculated as:

$$\rho_\Gamma = \frac{1}{N^{3/4}} \sum_i \rho_i, \tag{A1}$$

where $i$ runs over all the pixels in a track and N is the total number of pixels in it. These are then ranked and the track with largest $\rho_\Gamma$ is picked as the trigger for a map. This is done for both the main on-source search and for the background estimation over time-shifted data.

*Background triggers and loudest events*—Fig. 4 shows the distribution of false alarm probabilities $p_{\rm FA}$ for the SNRs of triggers collected in background data, for both high- and low-frequency spectrograms. The loudest on-source event in each frequency range is also shown.

### A.2. *HMM tracking*

A general description of the HMM method is given by Suvorova et al. (2016) and Sun et al. (2018). The following summary is intended to clarify the configuration used for the search presented in this paper.

*Probabilistic model*—A Markov chain is a stochastic process transitioning between discrete states at discrete times $\{t_0, \cdots, t_{N_T}\}$. A HMM is an automaton based on a Markov chain, composed of the hidden (unmeasurable) state variable $q(t) \in \{q_1, \cdots, q_{N_Q}\}$ and the measurement variable $o(t) \in \{o_1, \cdots, o_{N_O}\}$. A HMM is memoryless, i.e., the hidden state at time $t_{n+1}$ only depends on the state at time $t_n$, with transition probability

$$A_{q_j q_i} = P[q(t_{n+1}) = q_j | q(t_n) = q_i]. \tag{A2}$$

The hidden state $q_i$ is in observed state $o_j$ at time $t_n$ with emission probability

$$L_{o_j q_i} = P[o(t_n) = o_j | q(t_n) = q_i]. \tag{A3}$$

Given the prior defined by

$$\Pi_{q_i} = P[q(t_0) = q_i], \tag{A4}$$

the probability that the hidden state path $Q = \{q(t_0), \cdots, q(t_{N_T})\}$ gives rise to the observed sequence $O = \{o(t_0), \cdots, o(t_{N_T})\}$ equals

$$P(Q|O) = L_{o(t_{N_T})q(t_{N_T})} A_{q(t_{N_T})q(t_{N_T-1})} \cdots L_{o(t_1)q(t_1)} A_{q(t_1)q(t_0)} \Pi_{q(t_0)}. \tag{A5}$$

The most probable path

$$Q^*(O) = \arg\max P(Q|O), \tag{A6}$$

maximizes $P(Q|O)$ and gives the best estimate of $q(t)$ over the total observation, where $\arg\max(\cdots)$ returns the argument that maximizes the function $(\cdots)$. We use the classic Viterbi algorithm (Viterbi 1967) to efficiently solve the HMM and compute $Q^*(O)$.

*Search setup*—In this analysis, we track $q(t) = f_{\rm gw}(t)$, where $f_{\rm gw}(t)$ is the GW signal frequency at time $t$. The discrete hidden states are mapped one-to-one to the frequency bins in the output of a frequency-domain estimator $G(f)$ computed over an interval of length $T_{\rm drift}$, with bin size $\Delta f$. We aim at searching for signals with $10^2\,{\rm s} \lesssim \tau \lesssim 10^4\,{\rm s}$, corresponding to $\dot{f}_{\rm gw} \lesssim 1\,{\rm Hz\,s^{-1}}$. We choose $T_{\rm drift} = 1\,{\rm s}$ (i.e., $\Delta f = 1\,{\rm Hz}$) to satisfy

$$\left| \int_t^{t+T_{\rm drift}} dt' \dot{f}_{\rm gw}(t') \right| \leq \Delta f \tag{A7}$$

for $0 \leq t \leq T_{\rm obs}$, where $T_{\rm obs}$ is the total observing time. The motion of the Earth with respect to the solar system barycenter (SSB) can be neglected during the interval $[t, t + T_{\rm drift}]$. Hence the emission probability $L_{o(t)q_i} = P[o(t)|f_i \leq f_{\rm gw}(t) \leq f_i + \Delta f] \propto \exp[G(f_i)]$ is calculated from the running-mean (window width 3 Hz) normalized power in SFTs with length $T_{\rm SFT} = T_{\rm drift} = 1\,{\rm s}$ as the estimator $G(f)$. We write

$$G(f_i) = \sum_X \tilde{y}_i^X \tilde{y}_i^{X*}, \tag{A8}$$

where $i$ indexes the frequency bins of the normalized SFT $\tilde{y}$, $X$ indexes the detector, and the repeated index $i$ on the right-hand side does not imply summation. We assume that the auto-correlation time-scale of timing noise is much longer than $T_{\rm drift}$, and hence adopt the transition probabilities

$$A_{q_{i-1}q_i} = A_{q_i q_i} = \frac{1}{2}, \tag{A9}$$

with all other entries being zero. Since we have no independent knowledge of $f_{\rm gw}$, we choose a uniform prior, viz.

$$\Pi_{q_i} = N_Q^{-1}. \tag{A10}$$

We define a detection statistic $\mathcal{P}$, given by

$$\mathcal{P} = \frac{1}{N_T + 1} \sum_{n=0}^{N_T} G[f_{i(t_n)}], \tag{A11}$$

where the integer $i(t_n)$ indexes the SFT frequency bin corresponding to $q^*(t_n)$ on the optimal path $Q^*$ ($t_0 \leq t_n \leq t_{N_T}$).

The strain amplitude $h_0$ in (4) decreases significantly for $t \gg \tau$. Hence the instant SNR decreases for $T_{\rm obs} \gtrsim \tau$. Monte-Carlo simulations show that choosing $T_{\rm obs} \sim \tau$ yields the best sensitivities for signals with $h_0$ (Eq. 4) near the detection limit for the waveform in Eq. 3.

The initial spin-down rate $|\dot{f}_{\rm gw0}|$ of a signal with $\tau \lesssim 10^3\,{\rm s}$ can be too high (i.e., $|\dot{f}_{\rm gw0}| > 1\,{\rm Hz\,s^{-1}}$) for Eqn. (A7) to be satisfied with $T_{\rm drift} = 1\,{\rm s}$. We start the search after waiting for a time $t_{\rm wait}$ post-merger, when $\dot{f}_{\rm gw}|$ decreases such that Eqn. (A7) is satisfied. Alternatively, we can choose shorter $T_{\rm drift}$ (i.e., $T_{\rm drift} \leq \dot{f}_{\rm gw}^{-1/2}$) and take $t_{\rm wait} = 0$ for all waveforms. However, the sensitivity degrades because the frequency resolution $\Delta f > 1\,{\rm Hz}$ is relatively coarse for $T_{\rm drift} < 1\,{\rm s}$.

In a search without prior knowledge of the signal model, we cover the following parameter space $500\,{\rm Hz} \leq f_{\rm gw0} \leq 2\,{\rm kHz}$ for $10^2\,{\rm s} \lesssim \tau \lesssim 10^4\,{\rm s}$ using seven discrete $t_{\rm wait}$ values in the range $0 \leq t_{\rm wait} \leq 400\,{\rm s}$. Monte-Carlo simulations show that the impact on sensitivity from the mismatch in $t_{\rm wait}$ caused by the granularity is negligible.

### A.3. *Adaptive Transient Hough*

Here we summarize some key technical details concerning the search at hand, while the complete derivation of the search method is in Oliver et al. (2019).

*Coherence times*—The first step is selecting the coherent integration time $T_{\rm SFT}$, i.e. the time-baseline of the SFTs. This cannot be arbitrarily large: to avoid the signal shifting more than half a frequency bin, $T_{\rm SFT}$ must satisfy $|\dot{f}_{\rm gw}|T_{\rm SFT} \leq 1/(2T_{\rm SFT})$. The time variation of $f_{\rm gw}(t)$ is due to two effects: the spin-down of the source, and the Doppler modulation due to the Earth's motion. It is important to notice that in contrast to the continuous wave case this method assumes that the Doppler modulation is a subdominant effect. Thus $T_{\rm SFT}$ can be estimated as:

$$T_{\rm SFT} \leq \frac{\sqrt{(n-1)\tau}}{\sqrt{2f_{\rm gw0}}} \tag{A12}$$

*Hough transform*—Second, each of these SFTs is digitized by setting a threshold $\rho_{\rm th}$ on the normalized power, that is directly related to the false alarm rate $\alpha$ and false dismissal rate $\beta$ of the search; the optimal value is 1.6 as derived in Krishnan et al. (2004). This digitized spectrum is then weighted based on the noise floor of the detector and the amplitude modulation of the source. The derivation of the weights is given in Oliver et al. (2019) and in Sintes & Krishnan (2007) for the CW all-sky case.

*Detection statistic and significance threshold*—Finally, each template—defined by the set of signal parameters $(f_{\rm gw0}, n, \tau)$—is incoherently integrated through the appropriate summation, known as the number count, over the weighted digitized spectrum following Eq. 3. The critical ratio $\Psi$ is defined to evaluate the significance of a given template, based on the results obtained for the weighted number count and its estimates over Gaussian noise for the mean $\mu$ and the standard deviation $\sigma$:

$$\Psi = \frac{n-\mu}{\sigma} = \frac{\sum_{i=1}^{N_{\rm SFTs}} w_i y_i - \sum_{i=1}^{N_{\rm SFTs}} w_i \alpha}{\sqrt{\sum_{i=1}^{N_{\rm SFTs}} w_i^2\, \alpha\,(1-\alpha)}} \tag{A13}$$

Here, $y_i$ corresponds to the $ith$ digitalized bin in a given templated track, $N_{\rm SFTs}$ is the number of SFTs and the weights are $w_i \propto (f_{{\rm gw},i})^{2m}(a_i^2 + b_i^2)/S_{{\rm n},i}$, where $a_i$ and $b_i$ are amplitude functions of the antenna pattern found in (Jaranowski et al. 1998) at the $i^{\rm th}$ time step and $S_{{\rm n},i}$ is the power spectral density at that given bin. As mentioned in Sintes & Krishnan (2007) and Oliver et al. (2019), any change in the normalization of the weights $w_i$ will not change the resulting sensitivity and will also leave significances, or critical ratios $\Psi$, unchanged. As shown in Oliver et al. (2019), the critical ratio for a multi-detector search can be written as

$$\Psi_{\rm m} = \sum_{k=1}^{N_{\rm det}} \Psi_k r_k \tag{A14}$$

where $r_k$ is each detector's relative contribution ratio—proportional to the number of SFTs, the noise power spectral density, the antenna pattern and the signal amplitude pattern— and $N_{\rm det}$ is the number of detectors. For detection purposes, a threshold is placed on the two-detector $\Psi_{\rm m}$ corresponding to a $5\sigma$ false alarm probability for the entire template bank. An additional single-detector threshold, used for a consistency veto step, is extrapolated from the $5\sigma$ threshold on $\Psi_{\rm m}$, to make the veto safer under consideration of the actual differences in $r_k$ for this data set.

*Candidate follow-up*—To verify that the 51 outliers found in the initial search step were produced by noise in the detector, and exclude the possiblility of having any actual astrophysical signals among them, we performed an additional follow-up step. For each template corresponding to one of the outliers, an analoguous analysis was performed but with the template $f_{\rm gw}(t)$ evolution starting instead 1 hour after the merger. From Eq. 3, templates starting at merger time have vanishing overlap with these +1 hour delayed versions of themselves. For all outliers, we find that the +1 hour critical ratios are compatible with the results found in the original search within $8\%$. Given the $5\sigma$ false-alarm threshold imposed, the critical ratio for these templates can be considered as stationary non-Gaussian noise with a false dismissal probability of less that $10^{-4}$.

### A.4. *Generalized FrequencyHough*

Full details of the adaptation of the FrequencyHough algorithm (Astone et al. 2014) to the case of rapid-spindown postmerger signals are given in Miller et al. (2018). Here we summarize some technical details relevant to the search presented in this paper.

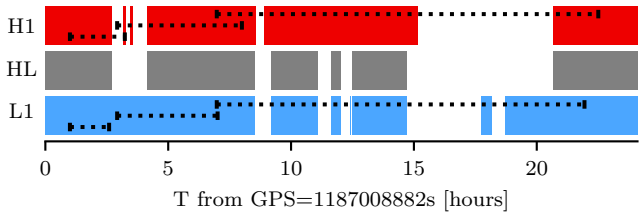


**Fig. 5.** FreqHough: Three configurations with different $T_{\mathrm{SFT}} = 2, 4, 8$ were used to search for a signal starting at least one hour to about 20 hours after the merger. The configurations were constructed to maximize sensitivity in different portions of the parameter space. We analyze the same amount of usable data in each detector, regardless of gaps in either detector's data, leading to later end times for the H1 detector in these three cases.

*Time offsets and search durations*—The search is run in three configurations using varying $T_{\mathrm{SFT}} = 2, 4, 8$ s, covering different observing times: $\Delta t = 1$ hour after merger with $T_{\mathrm{SFT}} = 2$ s for signals lasting 700-7000 s, $\Delta t \sim 1.5$–3 hours after merger with $T_{\mathrm{SFT}} = 4$ s for signals lasting 2000-16000 s, and $\Delta t \sim 2$–7 hours after merger with $T_{\mathrm{SFT}} = 8$ s for signals lasting 8000-40000 s. The corresponding end times are set separately for each detector to guarantee that the same effective amount of data is covered even in the presence of gaps; the latest timestamps analysed for either detector are approximately 3, 8 and 22 hours after merger in the three configurations. See Fig. 5.

*Coordinate transformation*—The parameters of the powerlaw spindown model are transformed to new coordinates, such that in the new space, the behavior of the signal is linear. If we write $k' = (2\pi)^{n-1}k$, we can rewrite Eq. 3 as:

$$f_{\mathrm{gw}}(t) = \frac{f_{\mathrm{start}}}{\left[1 + k'(n-1)f_{\mathrm{start}}^{n-1}(t - t_{ref})\right]^{\frac{1}{n-1}}} \tag{A15}$$

where:

$$k' = \frac{1}{\tau f_{\mathrm{start}}^{n-1}(n-1)}\,. \tag{A16}$$

Then we can make the following change of coordinates:

$$x = \frac{1}{f_{\mathrm{gw}}^{n-1}}; \quad x_0 = \frac{1}{f_{\mathrm{start}}^{n-1}}\,. \tag{A17}$$

Equation A15 becomes the equation of a line:

$$x = x_0 + (n-1)k'(t - t_0) \tag{A18}$$

Now, we map peaks in the $(t - t_0, f_{\mathrm{gw}})$ plane of the detector to lines in the $(x_0,k)$ plane of the source, where both variables in this space relate to the physical parameters of the source.

*Grid setup*—Our method can be used to determine if a signal is present in the data and estimate its $f_{\mathrm{start}}$, $\dot{f}_{\mathrm{start}}$ and $n$. We search across different braking indices with a fine, nonuniform grid determined by ensuring that by stepping from $n$ to $n + dn$, a signal is confined to one frequency bin. For each braking index, we do a Hough transform and record the most significant candidates in the map. The grid in $x_0$ is determined by taking the derivative of equation A17; the grid in $k$ is created by considering a transformation $f_{\mathrm{gw}} \to f_{\mathrm{gw}} + df_{\mathrm{gw}} = 1/T_{\mathrm{SFT}}$ and $k \to k + dk$, then solving for $dk$ imposing that the spindown remains constant.

Both grids are nonuniform and depend on the frequency band and spindown range we use; however, we overresolve the grid in $x_0$ for most frequency bands using the maximum frequency we are analyzing because it is computationally faster and doesn't result in a sensitivity loss.

The transformation has the disadvantage that it creates nonuniform noise (so peaks at higher frequencies contribute more to the Hough map). We account for this by extending the frequency band we wish to analyze, then only selecting candidates from the original band.

*Coincidence step*—Candidates are considered in coincidence between detectors if the Euclidean distance between their recovered parameters $x_0$ and $k$ is less than 3 bins.

*Candidate follow-up*—Our candidate follow-up procedure is the following: we correct for the phase evolution of the candidate recovered in each detector individually. Ideally, if we correct for exactly the right parameters, we expect a monochromatic signal in the time/frequency peakmap. If we are a bin or so off, there is a residual spindown or spinup, but the signal is linear. Therefore, we can apply the original FrequencyHough to search for this signal. After applying the original FrequencyHough to the one surviving candidate from this search and performing coincidences again, we found no coincidence, indicating that the candidate was false. We use the critical ratio as a way to veto candidates, defined as:

$$CR = \frac{y - \mu}{\sigma} \tag{A19}$$

where $y$ is the number count in a given bin in the Hough map, $\mu$ is the average number count of the noise, and $\sigma$ is the standard deviation of the number counts due to noise. We determine if the critical ratio increases in the follow-up, but find that it does not for our one remaining candidate.

*Sensitivity estimation procedure*—We then computed the strain sensitivity for the different configuations of our search in the following way: the loudest coincident candidate was selected in each 50 Hz band, for $n = 5$. Its $f_{\rm start}$ and duration were used to inject signals with initial frequencies ranging from $f_{\rm start}$ to $f_{\rm start} + 50$ Hz, with the highest possible spindown in our configuration $\dot{f}_{\rm start} = 1/T^2_{\rm SFT}$. Based on our theoretical estimates for sensitivity, the highest initial spindown corresponds to the most conservative result, i.e. the worst case sensitivity. 100 injections were done for each set of parameters, i.e. each point plotted in Figs. 2, 3 and 9 and each row in Table 5. Recovery of an injection is defined in the same way as a dection in the real search: within a coincidence distance of 3 bins.

## B. DETAILS ON PIPELINE SENSITIVITY

In Figures 6–9 and Tables 2–5 we summarize the full sensitivity estimates performed for each of the four pipelines with their respective injection sets of simulated signals following the power-law spin-down model (Eq. 3) with $n = 5$. Additional details on the injection sets and sensitivity estimation procedure for each pipeline are given in the previous section or, where necessary, in the table captions.

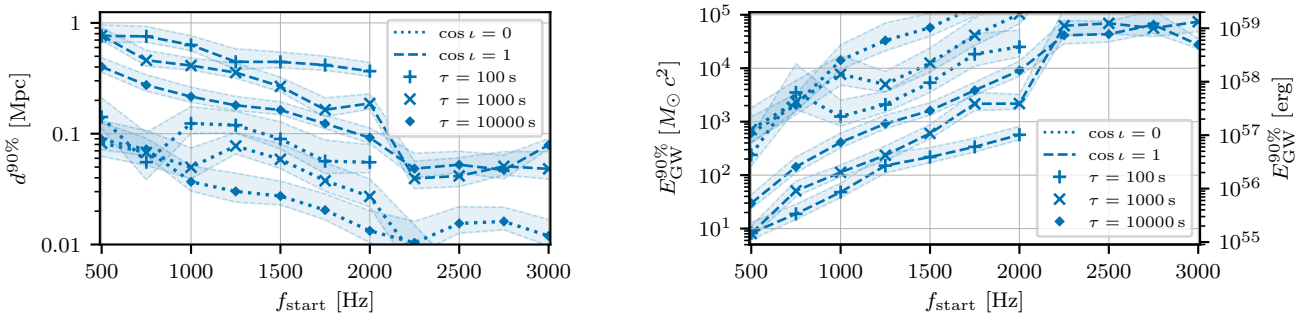


**Fig 6.** STAMP 90% sensitivity estimates for $n = 5$ and variable $f_{\mathrm{start}}$. For either $\cos\iota = [0, 1]$, the connected lines (from top to bottom in $d$) are for injections with $\tau \in [10^2, 10^3, 10^4]$ s. Shaded ranges correspond to $1\sigma$ binomial counting errors on the injection sets.

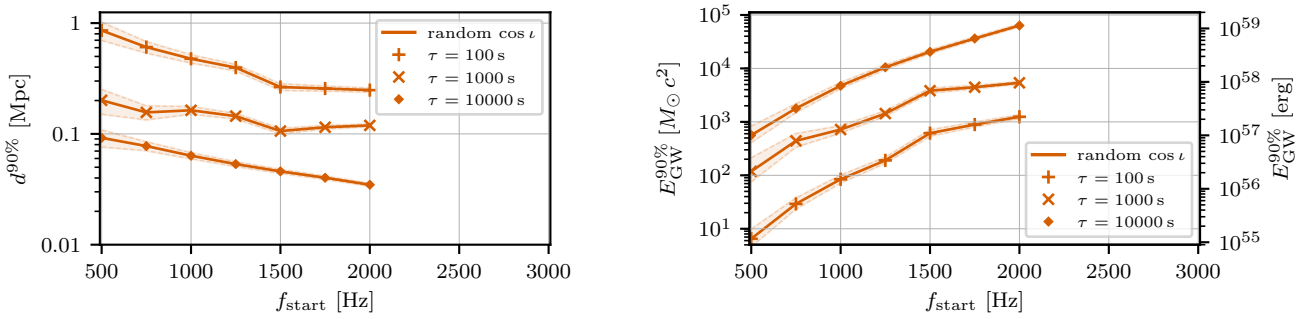


**Fig 7.** HMM 90% sensitivity estimates for $n = 5$ and $f_{\mathrm{start}} = f_{\mathrm{gw0}} = f_{\mathrm{gw}}(t_{\mathrm{c}})$. The connected lines (from top to bottom in $d$) are for injections with $\tau \in [10^2, 10^3, 10^4]$ s. Shaded ranges illustrate the uncertainty due to interpolating discrete steps in injection amplitudes.

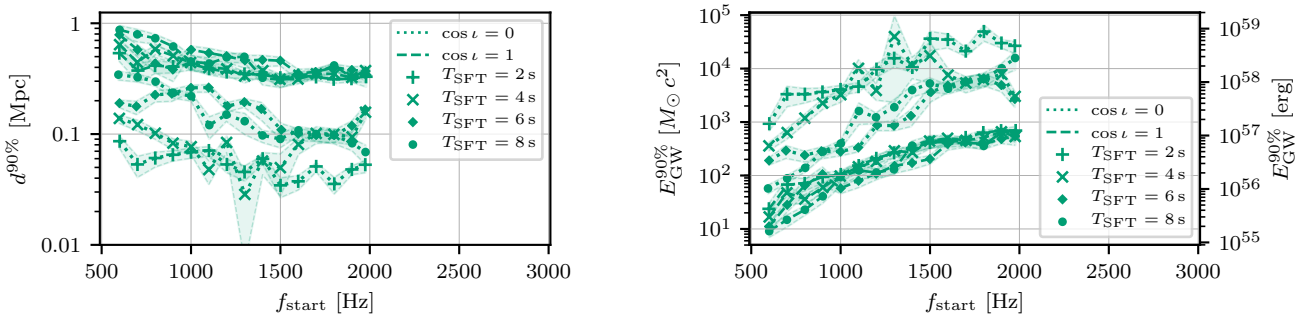


**Fig 8.** ATrHough 90% sensitivity estimates for $n = 5$ and $f_{\mathrm{start}} = f_{\mathrm{gw0}} = f_{\mathrm{gw}}(t_{\mathrm{c}})$. For either $\cos\iota = [0, 1]$, the connected lines (from bottom to top in $d$) are for coherence times of $T_{\mathrm{SFT}} = [2, 4, 6, 8]$. Shaded ranges: $2\sigma$ envelopes of logit fits over the different injection sets.

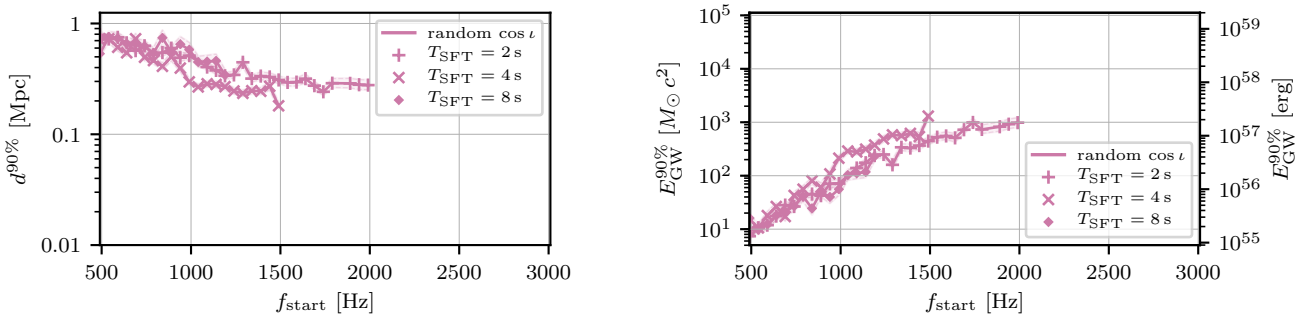


**Fig 9.** FreqHough 90% sensitivity estimates for $n = 5$ and $f_{\mathrm{start}} = f_{\mathrm{gw}}(t_{\mathrm{start}} = t_{\mathrm{c}} + \Delta t)$. The connected lines are for coherence times of $T_{\mathrm{SFT}} = [2, 4, 8]$ s. Shaded ranges give the uncertainty due to interpolating discrete steps in injection amplitudes.

**E2.** STAMP search sensitivities estimated from simulated signals (injections) following the power-law spindown model with braking index $n = 5$. Each row corresponds to an injection set with fixed parameters; sensitivities are at 90% confidence.

| $\cos\iota$ | $f_{\rm gw0}$ [Hz] | $\tau$ [s] | $\epsilon$ | $d^{90\%}$ [Mpc] | $E_{\rm gw}^{90\%}$ $[M_\odot c^2]$ |
|---|---|---|---|---|---|
| 0.0 | 500 | $1.00 \times 10^2$ | $7.33 \times 10^{-2}$ | $0.14^{+0.07}_{-0.03}$ | $2.39^{+2.85}_{-0.88} \times 10^2$ |
| 0.0 | 750 | $1.00 \times 10^2$ | $3.26 \times 10^{-2}$ | $0.055^{+0.047}_{-0.017}$ | $3.52^{+8.43}_{-1.80} \times 10^3$ |
| 0.0 | 1000 | $1.00 \times 10^2$ | $1.83 \times 10^{-2}$ | $0.12^{+0.05}_{-0.02}$ | $1.25^{+1.25}_{-0.42} \times 10^3$ |
| 0.0 | 1250 | $1.00 \times 10^2$ | $1.17 \times 10^{-2}$ | $0.12^{+0.04}_{-0.02}$ | $2.10^{+1.57}_{-0.58} \times 10^3$ |
| 0.0 | 1500 | $1.00 \times 10^2$ | $8.14 \times 10^{-3}$ | $0.090^{+0.038}_{-0.017}$ | $5.36^{+5.45}_{-1.81} \times 10^3$ |
| ... | ... | ... | ... | ... | ... |

NOTE—Full table available as online machine-readable version.

## REFERENCES


Aasi, J., et al. 2014, CQGra, 31, 085014

—. 2015a, CQGra, 32, 074001

—. 2015b, ApJ, 813, 39

Abbott, B. P., et al. 2017a, PhRvD, 96, 062002

—. 2017b, CQGra, 34, 044001

—. 2017c, ApJL, 848, L13

—. 2017d, PhRvL, 119, 141101

—. 2017e, ApJL, 848, L12

—. 2017f, PhRvD, 95, 122003

—. 2017g, ApJL, 851, L16

—. 2018a, CQGra, 35, 065009

—. 2018b, PhRvD, 97, 102003

—. 2018c, PhRvL, 121, 161101

—. 2018d, Living Rev. Rel., 21:3, arXiv:1304.0670

—. 2019, PhRvX, 9, 011001

Acernese, F., et al. 2015, CQGra, 32, 024001

Ai, S., Gao, H., Dai, Z.-G., et al. 2018, ApJ, 860, 57

Alford, M. G., & Schwenzer, K. 2014, ApJ, 781, 26

—. 2015, MNRAS, 446, 3631

Antonucci, F., Astone, P., D'Antonio, S., Frasca, S., & Palomba, C. 2008, CQGra, 25, 184015

Arras, P., Flanagan, E. E., Morsink, S. M., et al. 2003, ApJ, 591, 1129

Astone, P., Colla, A., D'Antonio, S., Frasca, S., & Palomba, C. 2014, PhRvD, 90, 042002

Baiotti, L., & Rezzolla, L. 2017, Rept. Prog. Phys., 80, 096901

Barsotti, L., McCuller, L., Evans, M., & Fritschel, P. 2018, The A+ design curve, Tech. Rep. LIGO-T1800042

Bauswein, A., Just, O., Janka, H.-T., & Stergioulas, N. 2017, ApJL, 850, L34

Bondarescu, R., Teukolsky, S. A., & Wasserman, I. 2009, PhRvD, 79, 104003

Cahillane, C., et al. 2017, PhRvD, 96, 102001

Coulter, D. A., et al. 2017, Science, 358, 1556

Covas, P., et al. 2018, PhRvD, 97, 082002

Cutler, C. 2002, PhRvD, 66, 084025

Dall'Osso, S., Giacomazzo, B., Perna, R., & Stella, L. 2015, ApJ, 798, 25

Dall'Osso, S., Shore, S. N., & Stella, L. 2009, MNRAS, 398, 1869

Dall'Osso, S., Stella, L., & Palomba, C. 2018, MNRAS, 480, 1353

Davis, D., Massinger, T. J., Lundgren, A. P., et al. 2019, CQGra, 36, 055011

Dooley, K. L., et al. 2016, CQGra, 33, 075009

Driggers, J. C., et al. 2019, PhRvD, 99, 042001

Freedman, W. L., et al. 2001, ApJ, 553, 47

Geng, J.-J., Dai, Z.-G., Huang, Y.-F., et al. 2018, ApJL, 856, L33

Granot, J., Gill, R., Guetta, D., & De Colle, F. 2018, MNRAS, 481, 1597

Granot, J., Guetta, D., & Gill, R. 2017, ApJL, 850, L24

Hild, S., et al. 2011, CQGra, 28, 094013

Hjorth, J., Levan, A. J., Tanvir, N. R., et al. 2017, ApJL, 848, L31

Jaranowski, P., Królak, A., & Schutz, B. F. 1998, PhRvD, 58, 063001

Johnson-McDaniel, N. K., & Owen, B. J. 2013, PhRvD, 88, 044004

Kasen, D., Metzger, B., Barnes, J., Quataert, E., & Ramirez-Ruiz, E. 2017, Nature, 551, 80

Keitel, D. 2016, PhRvD, 93, 084024

Krishnan, B., Sintes, A. M., Papa, M. A., et al. 2004, PhRvD, 70, 082001

**13.** HMM search sensitivities estimated from simulated signals (injections) following the power-law spindown model with braking index $n = 5$. Each row corresponds to injections marginalized over random $\cos\iota$; sensitivities are at 90% confidence.

| $f_{\rm gw0}$ [Hz] | $\tau$ [s] | $\epsilon$ | $d^{90\%}$ [Mpc] | $E_{\rm gw}^{90\%}$ $[M_\odot c^2]$ |
|---|---|---|---|---|
| 500 | $1.00 \times 10^{2}$ | $7.33 \times 10^{-2}$ | $0.86^{+0.16}_{-0.16}$ | $6.51^{+3.29}_{-1.87} \times 10^{0}$ |
| 750 | $1.00 \times 10^{2}$ | $3.26 \times 10^{-2}$ | $0.61^{+0.07}_{-0.07}$ | $2.92^{+0.82}_{-0.58} \times 10^{1}$ |
| 1000 | $1.00 \times 10^{2}$ | $1.83 \times 10^{-2}$ | $0.48^{+0.04}_{-0.04}$ | $8.43^{+1.60}_{-1.25} \times 10^{1}$ |
| 1250 | $1.00 \times 10^{2}$ | $1.17 \times 10^{-2}$ | $0.40^{+0.03}_{-0.03}$ | $1.90^{+0.27}_{-0.22} \times 10^{2}$ |
| 1500 | $1.00 \times 10^{2}$ | $8.14 \times 10^{-3}$ | $0.26^{+0.02}_{-0.02}$ | $6.15^{+0.91}_{-0.75} \times 10^{2}$ |
| ... | ... | ... | ... | ... |

NOTE—Full table available as online machine-readable version.

**14.** ATrHough search sensitivities estimated from simulated signals (injections) following the power-law spindown model with braking index $n = 5$. Each row corresponds to injections marginalized over a small band in $f_{\rm gw0}$; sensitivities are at 90% confidence.

| $T_{\rm SFT}$ [s] | $\cos\iota$ | $f_{\rm gw0}$ [Hz] | $\tau$ [s] | $\epsilon$ | $d^{90\%}$ [Mpc] | $E_{\rm gw}^{90\%}$ $[M_\odot c^2]$ |
|---|---|---|---|---|---|---|
| 2 | 0.0 | 601 | $6.01 \times 10^{2}$ | $2.07 \times 10^{-2}$ | $0.086^{+0.009}_{-0.012}$ | $9.30^{+1.96}_{-2.32} \times 10^{2}$ |
| 2 | 0.0 | 700 | $7.00 \times 10^{2}$ | $1.41 \times 10^{-2}$ | $0.053^{+0.010}_{-0.012}$ | $3.32^{+1.29}_{-1.37} \times 10^{3}$ |
| 2 | 0.0 | 800 | $8.00 \times 10^{2}$ | $1.01 \times 10^{-2}$ | $0.061^{+0.008}_{-0.010}$ | $3.32^{+0.89}_{-1.03} \times 10^{3}$ |
| 2 | 0.0 | 898 | $8.98 \times 10^{2}$ | $7.57 \times 10^{-3}$ | $0.065^{+0.006}_{-0.008}$ | $3.66^{+0.65}_{-0.81} \times 10^{3}$ |
| 2 | 0.0 | 1000 | $1.00 \times 10^{3}$ | $5.80 \times 10^{-3}$ | $0.069^{+0.006}_{-0.008}$ | $4.07^{+0.73}_{-0.89} \times 10^{3}$ |
| ... | ... | ... | ... | ... | ... | ... |

NOTE—Full table available as online machine-readable version.

**15.** FreqHough search sensitivities estimated from simulated signals (injections) following the power-law spindown model with braking index $n = 5$. Each row corresponds to injections marginalized over a 50 Hz band in $f_{\rm start}$ (where $f_{\rm start} = f_{\rm gw}(t_{\rm start} = t_{\rm c} + \Delta t)$) and random $\cos\iota$; sensitivities are at 90% confidence.

| $T_{\rm SFT}$ [s] | $f_{\rm start}$ [Hz] | $\tau$ [s] | $\epsilon$ | $d^{90\%}$ [Mpc] | $E_{\rm gw}^{90\%}$ $[M_\odot c^2]$ |
|---|---|---|---|---|---|
| 2 | 390 | $4.15 \times 10^{2}$ | $5.91 \times 10^{-2}$ | $0.78^{+0.05}_{-0.04}$ | $4.76^{+0.59}_{-0.50} \times 10^{0}$ |
| 2 | 440 | $4.65 \times 10^{2}$ | $4.39 \times 10^{-2}$ | $0.83^{+0.06}_{-0.05}$ | $5.42^{+0.75}_{-0.62} \times 10^{0}$ |
| 2 | 490 | $5.15 \times 10^{2}$ | $3.36 \times 10^{-2}$ | $0.79^{+0.06}_{-0.05}$ | $7.39^{+1.08}_{-0.89} \times 10^{0}$ |
| 2 | 540 | $5.65 \times 10^{2}$ | $2.64 \times 10^{-2}$ | $0.72^{+0.05}_{-0.04}$ | $1.06^{+0.15}_{-0.12} \times 10^{1}$ |
| 2 | 590 | $6.15 \times 10^{2}$ | $2.12 \times 10^{-2}$ | $0.75^{+0.06}_{-0.05}$ | $1.19^{+0.20}_{-0.16} \times 10^{1}$ |
| ... | ... | ... | ... | ... | ... |

NOTE—Full table available as online machine-readable version.

Lasky, P. D., Sarin, N., & Sammut, L. 2017, Long-duration waveform models for millisecond magnetars born in binary neutron star mergers, Tech. Rep. LIGO-T1700408
Lee, M. G., Kang, J., & Im, M. 2018, ApJL, 859, L6
Li, S.-Z., Liu, L.-D., Yu, Y.-W., & Zhang, B. 2018, ApJL, 861, L12
Margalit, B., & Metzger, B. D. 2017, ApJL, 850, L19
Matsumoto, T., Ioka, K., Kisaka, S., & Nakar, E. 2018, ApJ, 861, 55
Messenger, C., et al. 2015, PhRvD, 92, 023006
Miller, A., Astone, P., D'Antonio, S., et al. 2018, PhRvD, 98, 102004
Oliver, M., Keitel, D., & Sintes, A. M. 2019, arXiv:1901.01820
Owen, B. J., Lindblom, L., Cutler, C., et al. 1998, PhRvD, 58, 084020
Palomba, C. 2001, A&A, 367, 525
Palomba, C., Astone, P., & Frasca, S. 2005, CQGra, 22, S1255
Piro, A. L., Giacomazzo, B., & Perna, R. 2017, ApJL, 844, L19
Pooley, D., Kumar, P., Wheeler, J. C., & Grossan, B. 2018, ApJL, 859, L23
Prix, R. 2009, in ASSL, Vol. 357, Neutron Stars and Pulsars, ed. W. Becker (Springer Berlin Heidelberg), 651–685
Prix, R., Giampanis, S., & Messenger, C. 2011, PhRvD, 84, 023007
Radice, D., Perego, A., Zappa, F., & Bernuzzi, S. 2018, ApJL, 852, L29
Ravi, V., & Lasky, P. D. 2014, MNRAS, 441, 2433
Reisenegger, A. 2009, A&A, 499, 557
Rezzolla, L., Most, E. R., & Weih, L. R. 2018, ApJL, 852, L25
Riles, K. 2017, Mod. Phys. Lett., A32, 1730035
Sakai, S., et al. 2000, ApJ, 529, 698
Sarin, N., Lasky, P. D., Sammut, L., & Ashton, G. 2018, PhRvD, 98, 043011
Sathyaprakash, B., et al. 2012, CQGra, 29, 124013
Shapiro, S. L., & Teukolsky, S. A. 1983, Black holes, white dwarfs, and neutron stars: The physics of compact objects (Wiley, New York)
Sintes, A. M., & Krishnan, B. 2007, Hough search with improved sensitivity, Tech. Rep. LIGO-T070124
Sun, L., & Melatos, A. 2018, arXiv:1810.03577
Sun, L., Melatos, A., Lasky, P., Chung, C., & Darman, N. 2016, PhRvD, 94, 082004
Sun, L., Melatos, A., Suvorova, S., Moran, W., & Evans, R. 2018, PhRvD, D97, 043013
Suvorova, S., Sun, L., Melatos, A., Moran, W., & Evans, R. J. 2016, PhRvD, D93, 123009
Thrane, E., & Coughlin, M. 2013, PhRvD, 88, 083010
Thrane, E., Mandic, V., & Christensen, N. 2015, PhRvD, 91, 104021
Thrane, E., et al. 2011, PhRvD, 83, 083004
van Putten, M. H. P. M., & Della Valle, M. 2018, MNRAS, 482, L46
Viterbi, A. 1967, IEEE Transactions on Information Theory, 13, 260
Walsh, S., et al. 2016, PhRvD, 94, 124010
Yu, Y.-W., Liu, L.-D., & Dai, Z.-G. 2018, ApJ, 861, 114
Zhu, S. J., et al. 2016, PhRvD, 94, 082008

THE LIGO SCIENTIFIC COLLABORATION, THE VIRGO COLLABORATION, B. P. ABBOTT,[1] R. ABBOTT,[1] T. D. ABBOTT,[2] F. ACERNESE,[3,4] K. ACKLEY,[5] C. ADAMS,[6] T. ADAMS,[7] P. ADDESSO,[8] R. X. ADHIKARI,[1] V. B. ADYA,[9,10] C. AFFELDT,[9,10] B. AGARWAL,[11] M. AGATHOS,[12] K. AGATSUMA,[13] N. AGGARWAL,[14] O. D. AGUIAR,[15] L. AIELLO,[16,17] A. AIN,[18] P. AJITH,[19] B. ALLEN,[9,20,10] G. ALLEN,[11] A. ALLOCCA,[21,22] M. A. ALOY,[23] P. A. ALTIN,[24] A. AMATO,[25] A. ANANYEVA,[1] S. B. ANDERSON,[1] W. G. ANDERSON,[20] S. V. ANGELOVA,[26] S. ANTIER,[27] S. APPERT,[1] K. ARAI,[1] M. C. ARAYA,[1] J. S. AREEDA,[28] M. ARÈNE,[29] N. ARNAUD,[27,30] S. ASCENZI,[31,32] G. ASHTON,[5] M. AST,[33] S. M. ASTON,[6] P. ASTONE,[34] D. V. ATALLAH,[35] F. AUBIN,[7] P. AUFMUTH,[10] C. AULBERT,[9] K. AULTONEAL,[36] C. AUSTIN,[2] A. AVILA-ALVAREZ,[28] S. BABAK,[37,29] P. BACON,[29] F. BADARACCO,[16,17] M. K. M. BADER,[13] S. BAE,[38] P. T. BAKER,[39] F. BALDACCINI,[40,41] G. BALLARDIN,[30] S. W. BALLMER,[42] S. BANAGIRI,[43] J. C. BARAYOGA,[1] S. E. BARCLAY,[44] B. C. BARISH,[1] D. BARKER,[45] K. BARKETT,[46] S. BARNUM,[14] F. BARONE,[3,4] B. BARR,[44] L. BARSOTTI,[14] M. BARSUGLIA,[29] D. BARTA,[47] J. BARTLETT,[45] I. BARTOS,[48] R. BASSIRI,[49] A. BASTI,[21,22] J. C. BATCH,[45] M. BAWAJ,[50,41] J. C. BAYLEY,[44] M. BAZZAN,[51,52] B. BÉCSY,[53] C. BEER,[9] M. BEJGER,[54] I. BELAHCENE,[27] A. S. BELL,[44] D. BENIWAL,[55] M. BENSCH,[9,10] B. K. BERGER,[1] G. BERGMANN,[9,10] S. BERNUZZI,[56,57] J. J. BERO,[58] C. P. L. BERRY,[59] D. BERSANETTI,[60] A. BERTOLINI,[13] J. BETZWIESER,[6] R. BHANDARE,[61] I. A. BILENKO,[62] S. A. BILGILI,[39] G. BILLINGSLEY,[1] C. R. BILLMAN,[48] J. BIRCH,[6] R. BIRNEY,[26] O. BIRNHOLTZ,[58] S. BISCANS,[1,14] S. BISCOVEANU,[5] A. BISHT,[9,10] M. BITOSSI,[30,22] M. A. BIZOUARD,[27] J. K. BLACKBURN,[1] J. BLACKMAN,[46] C. D. BLAIR,[6] D. G. BLAIR,[63] R. M. BLAIR,[45] S. BLOEMEN,[64] O. BOCK,[9] N. BODE,[9,10] M. BOER,[65] Y. BOETZEL,[66] G. BOGAERT,[65] A. BOHE,[37] F. BONDU,[67] E. BONILLA,[49] R. BONNAND,[7] P. BOOKER,[9,10] B. A. BOOM,[13] C. D. BOOTH,[35] R. BORK,[1] V. BOSCHI,[30] S. BOSE,[68,18] K. BOSSIE,[6] V. BOSSILKOV,[63] J. BOSVELD,[63] Y. BOUFFANAIS,[29] A. BOZZI,[30] C. BRADASCHIA,[22] P. R. BRADY,[20] A. BRAMLEY,[6] M. BRANCHESI,[16,17] J. E. BRAU,[69] T. BRIANT,[70] F. BRIGHENTI,[71,72] A. BRILLET,[65] M. BRINKMANN,[9,10] V. BRISSON,[27,*] P. BROCKILL,[20] A. F. BROOKS,[1] D. D. BROWN,[55] S. BRUNETT,[1] C. C. BUCHANAN,[2] A. BUIKEMA,[14] T. BULIK,[73] H. J. BULTEN,[74,13] A. BUONANNO,[37,75] D. BUSKULIC,[7] C. BUY,[29] R. L. BYER,[49] M. CABERO,[9] L. CADONATI,[76] G. CAGNOLI,[25,77] C. CAHILLANE,[1] J. CALDERÓN BUSTILLO,[76] T. A. CALLISTER,[1] E. CALLONI,[78,4] J. B. CAMP,[79] M. CANEPA,[80,60] P. CANIZARES,[64] K. C. CANNON,[81] H. CAO,[55] J. CAO,[82] C. D. CAPANO,[9] E. CAPOCASA,[29] F. CARBOGNANI,[30] S. CARIDE,[83] M. F. CARNEY,[84] J. CASANUEVA DIAZ,[22] C. CASENTINI,[31,32] S. CAUDILL,[13,20] M. CAVAGLIÀ,[85] F. CAVALIER,[27] R. CAVALIERI,[30] G. CELLA,[22] C. B. CEPEDA,[1] P. CERDÁ-DURÁN,[23] G. CERRETANI,[21,22] E. CESARINI,[86,32] O. CHAIBI,[65] S. J. CHAMBERLIN,[87] M. CHAN,[44] S. CHAO,[88] P. CHARLTON,[89] E. CHASE,[90] E. CHASSANDE-MOTTIN,[29] D. CHATTERJEE,[20] B. D. CHEESEBORO,[39] H. Y. CHEN,[91] X. CHEN,[63] Y. CHEN,[46] H.-P. CHENG,[48] H. Y. CHIA,[48] A. CHINCARINI,[60] A. CHIUMMO,[30] T. CHMIEL,[84] H. S. CHO,[92] M. CHO,[75] J. H. CHOW,[24] N. CHRISTENSEN,[93,65] Q. CHU,[63] A. J. K. CHUA,[46] S. CHUA,[70] K. W. CHUNG,[94] S. CHUNG,[63] G. CIANI,[51,52,48] A. A. CIOBANU,[55] R. CIOLFI,[95,96] F. CIPRIANO,[65] C. E. CIRELLI,[49] A. CIRONE,[80,60] F. CLARA,[45] J. A. CLARK,[76] P. CLEARWATER,[97] F. CLEVA,[65] C. COCCHIERI,[85] E. COCCIA,[16,17] P.-F. COHADON,[70] D. COHEN,[27] A. COLLA,[98,34] C. G. COLLETTE,[99] C. COLLINS,[59] L. R. COMINSKY,[100] M. CONSTANCIO JR.,[15] L. CONTI,[52] S. J. COOPER,[59] P. CORBAN,[6] T. R. CORBITT,[2] I. CORDERO-CARRIÓN,[101] K. R. CORLEY,[102] N. CORNISH,[103] A. CORSI,[83] S. CORTESE,[30] C. A. COSTA,[15] R. COTESTA,[37] M. W. COUGHLIN,[1] S. B. COUGHLIN,[35,90] J.-P. COULON,[65] S. T. COUNTRYMAN,[102] P. COUVARES,[1] P. B. COVAS,[104] E. E. COWAN,[76] D. M. COWARD,[63] M. J. COWART,[6] D. C. COYNE,[1] R. COYNE,[105] J. D. E. CREIGHTON,[20] T. D. CREIGHTON,[106] J. CRIPE,[2] S. G. CROWDER,[107] T. J. CULLEN,[2] A. CUMMING,[44] L. CUNNINGHAM,[44] E. CUOCO,[30] T. DAL CANTON,[79] G. DÁLYA,[53] S. L. DANILISHIN,[10,9] S. D'ANTONIO,[32] K. DANZMANN,[9,10] A. DASGUPTA,[108] C. F. DA SILVA COSTA,[48] V. DATTILO,[30] I. DAVE,[61] M. DAVIER,[27] D. DAVIS,[42] E. J. DAW,[109] B. DAY,[76] D. DEBRA,[49] M. DEENADAYALAN,[18] J. DEGALLAIX,[25] M. DE LAURENTIS,[78,4] S. DELÉGLISE,[70] W. DEL POZZO,[21,22] N. DEMOS,[14] T. DENKER,[9,10] T. DENT,[9] R. DE PIETRI,[56,57] J. DERBY,[28] V. DERGACHEV,[9] R. DE ROSA,[78,4] C. DE ROSSI,[25,30] R. DESALVO,[110] O. DE VARONA,[9,10] S. DHURANDHAR,[18] M. C. DÍAZ,[106] L. DI FIORE,[4] M. DI GIOVANNI,[111,96] T. DI GIROLAMO,[78,4] A. DI LIETO,[21,22] B. DING,[99] S. DI PACE,[98,34] I. DI PALMA,[98,34] F. DI RENZO,[21,22] A. DMITRIEV,[59] Z. DOCTOR,[91] V. DOLIQUE,[25] F. DONOVAN,[14] K. L. DOOLEY,[35,85] S. DORAVARI,[9,10] I. DORRINGTON,[35] M. DOVALE ÁLVAREZ,[59] T. P. DOWNES,[20] M. DRAGO,[9,16,17] C. DREISSIGACKER,[9,10] J. C. DRIGGERS,[45] Z. DU,[82] P. DUPEJ,[44] S. E. DWYER,[45] P. J. EASTER,[5] T. B. EDO,[109] M. C. EDWARDS,[93] A. EFFLER,[6] H.-B. EGGENSTEIN,[9,10] P. EHRENS,[1] J. EICHHOLZ,[1] S. S. EIKENBERRY,[48] M. EISENMANN,[7] R. A. EISENSTEIN,[14] R. C. ESSICK,[91] H. ESTELLES,[104] D. ESTEVEZ,[7] Z. B. ETIENNE,[39] T. ETZEL,[1] M. EVANS,[14] T. M. EVANS,[6] V. FAFONE,[31,32,16] H. FAIR,[42] S. FAIRHURST,[35] X. FAN,[82] S. FARINON,[60] B. FARR,[69] W. M. FARR,[59] E. J. FAUCHON-JONES,[35] M. FAVATA,[112] M. FAYS,[35] C. FEE,[84] H. FEHRMANN,[9] J. FEICHT,[1] M. M. FEJER,[49] F. FENG,[29] A. FERNANDEZ-GALIANA,[14] I. FERRANTE,[21,22] E. C. FERREIRA,[15] F. FERRINI,[30] F. FIDECARO,[21,22] I. FIORI,[30] D. FIORUCCI,[29] M. FISHBACH,[91] R. P. FISHER,[42] J. M. FISHNER,[14] M. FITZ-AXEN,[43] R. FLAMINIO,[7,113] M. FLETCHER,[44] H. FONG,[114] J. A. FONT,[23,115] P. W. F. FORSYTH,[24] S. S. FORSYTH,[76] J.-D. FOURNIER,[65] S. FRASCA,[98,34] F. FRASCONI,[22] Z. FREI,[53] A. FREISE,[59] R. FREY,[69] V. FREY,[27] P. FRITSCHEL,[14] V. V. FROLOV,[6] P. FULDA,[48] M. FYFFE,[6] H. A. GABBARD,[44] B. U. GADRE,[18] S. M. GAEBEL,[59] J. R. GAIR,[116] L. GAMMAITONI,[40] M. R. GANIJA,[55] S. G. GAONKAR,[18] A. GARCIA,[28] C. GARCÍA-QUIRÓS,[104] F. GARUFI,[78,4] B. GATELEY,[45] S. GAUDIO,[36] G. GAUR,[117] V. GAYATHRI,[118] G. GEMME,[60] E. GENIN,[30] A. GENNAI,[22] D. GEORGE,[11] J. GEORGE,[61] L. GERGELY,[119] V. GERMAIN,[7] S. GHONGE,[76] ABHIRUP GHOSH,[19] ARCHISMAN GHOSH,[13] S. GHOSH,[20] B. GIACOMAZZO,[111,96] J. A. GIAIME,[2,6] K. D. GIARDINA,[6] A. GIAZOTTO,[22,†] K. GILL,[36] G. GIORDANO,[3,4] L. GLOVER,[110] E. GOETZ,[45] R. GOETZ,[48] B. GONCHAROV,[5] G. GONZÁLEZ,[2] J. M. GONZALEZ CASTRO,[21,22] A. GOPAKUMAR,[120] M. L. GORODETSKY,[62] S. E. GOSSAN,[1] M. GOSSELIN,[30] R. GOUATY,[7] A. GRADO,[121,4] C. GRAEF,[44] M. GRANATA,[25] A. GRANT,[44] S. GRAS,[14] C. GRAY,[45] G. GRECO,[71,72] A. C. GREEN,[59] R. GREEN,[35] E. M. GRETARSSON,[36] P. GROOT,[64] H. GROTE,[35] S. GRUNEWALD,[37] P. GRUNING,[27] G. M. GUIDI,[71,72] H. K. GULATI,[108] X. GUO,[82] A. GUPTA,[87] M. K. GUPTA,[108] K. E. GUSHWA,[1] E. K. GUSTAFSON,[1] R. GUSTAFSON,[122] O. HALIM,[17,16] B. R. HALL,[68] E. D. HALL,[14] E. Z. HAMILTON,[35] H. F. HAMILTON,[123] G. HAMMOND,[44] M. HANEY,[66] M. M. HANKE,[9,10] J. HANKS,[45] C. HANNA,[87] M. D. HANNAM,[35] O. A. HANNUKSELA,[94] J. HANSON,[6] T. HARDWICK,[2] J. HARMS,[16,17] G. M. HARRY,[124] I. W. HARRY,[37] M. J. HART,[44] C.-J. HASTER,[114] K. HAUGHIAN,[44] J. HEALY,[58] A. HEIDMANN,[70] M. C. HEINTZE,[6] H. HEITMANN,[65] P. HELLO,[27] G. HEMMING,[30] M. HENDRY,[44] I. S. HENG,[44] J. HENNIG,[44] A. W. HEPTONSTALL,[1] F. J. HERNANDEZ,[5] M. HEURS,[9,10] S. HILD,[44] T. HINDERER,[64] D. HOAK,[30] S. HOCHHEIM,[9,10] D. HOFMAN,[25] N. A. HOLLAND,[24] K. HOLT,[6] D. E. HOLZ,[91] P. HOPKINS,[35] C. HORST,[20] J. HOUGH,[44] E. A. HOUSTON,[44] E. J. HOWELL,[63] A. HREIBI,[65] E. A. HUERTA,[11] D. HUET,[27] B. HUGHEY,[36] M. HULKO,[1]

S. Husa,[104] S. H. Huttner,[44] T. Huynh-Dinh,[6] A. Iess,[31,32] N. Indik,[9] C. Ingram,[55] R. Inta,[83] G. Intini,[98,34] H. N. Isa,[44] J.-M. Isac,[70] M. Isi,[1] B. R. Iyer,[19] K. Izumi,[45] T. Jacqmin,[70] K. Jani,[76] P. Jaranowski,[125] D. S. Johnson,[11] W. W. Johnson,[2] D. I. Jones,[126] R. Jones,[44] R. J. G. Jonker,[13] L. Ju,[63] J. Junker,[9,10] C. V. Kalaghatgi,[35] V. Kalogera,[90] B. Kamai,[1] S. Kandhasamy,[6] G. Kang,[38] J. B. Kanner,[1] S. J. Kapadia,[20] S. Karki,[69] K. S. Karvinen,[9,10] M. Kasprzack,[2] W. Kastaun,[9] M. Katolik,[11] S. Katsanevas,[30] E. Katsavounidis,[14] W. Katzman,[6] S. Kaufer,[9,10] K. Kawabe,[45] N. V. Keerthana,[18] F. Kéfélian,[65] D. Keitel,[44] A. J. Kemball,[11] R. Kennedy,[109] J. S. Key,[127] F. Y. Khalili,[62] B. Khamesra,[76] H. Khan,[28] I. Khan,[16,32] S. Khan,[9] Z. Khan,[108] E. A. Khazanov,[128] N. Kijbunchoo,[24] Chunglee Kim,[129] J. C. Kim,[130] K. Kim,[94] W. Kim,[55] W. S. Kim,[131] Y.-M. Kim,[132] E. J. King,[55] P. J. King,[45] M. Kinley-Hanlon,[124] R. Kirchhoff,[9,10] J. S. Kissel,[45] L. Kleybolte,[33] S. Klimenko,[48] T. D. Knowles,[39] P. Koch,[9,10] S. M. Koehlenbeck,[9,10] S. Koley,[13] V. Kondrashov,[1] A. Kontos,[14] M. Korobko,[33] W. Z. Korth,[1] I. Kowalska,[73] D. B. Kozak,[1] C. Krämer,[9] V. Kringel,[9,10] B. Krishnan,[9] A. Królak,[133,134] G. Kuehn,[9,10] P. Kumar,[135] R. Kumar,[108] S. Kumar,[19] L. Kuo,[88] A. Kutynia,[133] S. Kwang,[20] B. D. Lackey,[37] K. H. Lai,[94] M. Landry,[45] R. N. Lang,[136] J. Lange,[58] B. Lantz,[49] R. K. Lanza,[14] A. Lartaux-Vollard,[27] P. D. Lasky,[5] M. Laxen,[6] A. Lazzarini,[1] C. Lazzaro,[52] P. Leaci,[98,34] S. Leavey,[9,10] C. H. Lee,[92] H. K. Lee,[137] H. M. Lee,[129] H. W. Lee,[130] K. Lee,[44] J. Lehmann,[9,10] A. Lenon,[39] M. Leonardi,[9,10,113] N. Leroy,[27] N. Letendre,[7] Y. Levin,[5] J. Li,[82] T. G. F. Li,[94] X. Li,[46] S. D. Linker,[110] T. B. Littenberg,[138] J. Liu,[63] X. Liu,[20] R. K. L. Lo,[94] N. A. Lockerbie,[26] L. T. London,[35] A. Longo,[139,140] M. Lorenzini,[16,17] V. Loriette,[141] M. Lormand,[6] G. Losurdo,[22] J. D. Lough,[9,10] C. O. Lousto,[58] G. Lovelace,[28] H. Lück,[9,10] D. Lumaca,[31,32] A. P. Lundgren,[9] R. Lynch,[14] Y. Ma,[46] R. Macas,[35] S. Macfoy,[26] B. Machenschalk,[9] M. MacInnis,[14] D. M. Macleod,[35] I. Magaña Hernandez,[20] F. Magaña-Sandoval,[42] L. Magaña Zertuche,[85] R. M. Magee,[87] E. Majorana,[34] I. Maksimovic,[141] N. Man,[65] V. Mandic,[43] V. Mangano,[44] G. L. Mansell,[24] M. Manske,[20,24] M. Mantovani,[30] F. Marchesoni,[50,41] F. Marion,[7] S. Márka,[102] Z. Márka,[102] C. Markakis,[11] A. S. Markosyan,[49] A. Markowitz,[1] E. Maros,[1] A. Marquina,[101] F. Martelli,[71,72] L. Martellini,[65] I. W. Martin,[44] R. M. Martin,[112] D. V. Martynov,[14] K. Mason,[14] E. Massera,[109] A. Masserot,[7] T. J. Massinger,[1] M. Masso-Reid,[44] S. Mastrogiovanni,[98,34] A. Matas,[43] F. Matichard,[1,14] L. Matone,[102] N. Mavalvala,[14] N. Mazumder,[68] J. J. McCann,[63] R. McCarthy,[45] D. E. McClelland,[24] S. McCormick,[6] L. McCuller,[14] S. C. McGuire,[142] J. McIver,[1] D. J. McManus,[24] T. McRae,[24] S. T. McWilliams,[39] D. Meacher,[87] G. D. Meadors,[5] M. Mehmet,[9,10] J. Meidam,[13] E. Mejuto-Villa,[8] A. Melatos,[97] G. Mendell,[45] D. Mendoza-Gandara,[9,10] R. A. Mercer,[20] L. Mereni,[25] E. L. Merilh,[45] M. Merzougui,[65] S. Meshkov,[1] C. Messenger,[44] C. Messick,[87] R. Metzdorff,[70] P. M. Meyers,[43] H. Miao,[59] C. Michel,[25] H. Middleton,[97] E. E. Mikhailov,[143] L. Milano,[78,4] A. L. Miller,[48] A. Miller,[98,34] B. B. Miller,[90] J. Miller,[14] M. Millhouse,[103] J. Mills,[35] M. C. Milovich-Goff,[110] O. Minazzoli,[65,144] Y. Minenkov,[32] J. Ming,[9,10] C. Mishra,[145] S. Mitra,[18] V. P. Mitrofanov,[62] G. Mitselmakher,[48] R. Mittleman,[14] D. Moffa,[84] K. Mogushi,[85] M. Mohan,[30] S. R. P. Mohapatra,[14] M. Montani,[71,72] C. J. Moore,[12] D. Moraru,[45] G. Moreno,[45] S. Morisaki,[81] B. Mours,[7] C. M. Mow-Lowry,[59] G. Mueller,[48] A. W. Muir,[35] Arunava Mukherjee,[9,10] D. Mukherjee,[20] S. Mukherjee,[106] N. Mukund,[18] A. Mullavey,[6] J. Munch,[55] E. A. Muñiz,[42] M. Muratore,[36] P. G. Murray,[44] A. Nagar,[86,146,147] K. Napier,[76] I. Nardecchia,[31,32] L. Naticchioni,[98,34] R. K. Nayak,[148] J. Neilson,[110] G. Nelemans,[64,13] T. J. N. Nelson,[6] M. Nery,[9,10] A. Neunzert,[122] L. Nevin,[1] J. M. Newport,[124] K. Y. Ng,[14] S. Ng,[55] P. Nguyen,[69] T. T. Nguyen,[24] D. Nichols,[64] A. B. Nielsen,[9] S. Nissanke,[64,13] A. Nitz,[9] F. Nocera,[30] D. Nolting,[6] C. North,[35] L. K. Nuttall,[35] M. Obergaulinger,[23] J. Oberling,[45] B. D. O'Brien,[48] G. D. O'Dea,[110] G. H. Ogin,[149] J. J. Oh,[131] S. H. Oh,[131] F. Ohme,[9] H. Ohta,[81] M. A. Okada,[15] M. Oliver,[104] P. Oppermann,[9,10] Richard J. Oram,[6] B. O'Reilly,[6] R. Ormiston,[43] L. F. Ortega,[48] R. O'Shaughnessy,[58] S. Ossokine,[37] D. J. Ottaway,[55] H. Overmier,[6] B. J. Owen,[83] A. E. Pace,[87] G. Pagano,[21,22] J. Page,[138] M. A. Page,[63] A. Pai,[118] S. A. Pai,[61] J. R. Palamos,[69] O. Palashov,[128] C. Palomba,[34] A. Pal-Singh,[33] Howard Pan,[88] Huang-Wei Pan,[88] B. Pang,[46] P. T. H. Pang,[94] C. Pankow,[90] F. Pannarale,[35] B. C. Pant,[61] F. Paoletti,[22] A. Paoli,[30] M. A. Papa,[9,20,10] A. Parida,[18] W. Parker,[6] D. Pascucci,[44] A. Pasqualetti,[30] R. Passaquieti,[21,22] D. Passuello,[22] M. Patil,[134] B. Patricelli,[150,22] B. L. Pearlstone,[44] C. Pedersen,[35] M. Pedraza,[1] R. Pedurand,[25,151] L. Pekowsky,[42] A. Pele,[6] S. Penn,[152] C. J. Perez,[45] A. Perreca,[111,96] L. M. Perri,[90] H. P. Pfeiffer,[114,37] M. Phelps,[44] K. S. Phukon,[18] O. J. Piccinni,[98,34] M. Pichot,[65] F. Piergiovanni,[71,72] V. Pierro,[8] G. Pillant,[30] L. Pinard,[25] I. M. Pinto,[8] M. Pirello,[45] M. Pitkin,[44] R. Poggiani,[21,22] P. Popolizio,[30] E. K. Porter,[29] L. Possenti,[153,72] A. Post,[9] J. Powell,[154] J. Prasad,[18] J. W. W. Pratt,[36] G. Pratten,[104] V. Predoi,[35] T. Prestegard,[20] M. Principe,[8] S. Privitera,[37] G. A. Prodi,[111,96] L. G. Prokhorov,[62] O. Puncken,[9,10] M. Punturo,[41] P. Puppo,[34] M. Pürrer,[37] H. Qi,[20] V. Quetschke,[106] E. A. Quintero,[1] R. Quitzow-James,[69] F. J. Raab,[45] D. S. Rabeling,[24] H. Radkins,[45] P. Raffai,[53] S. Raja,[61] C. Rajan,[61] B. Rajbhandari,[83] M. Rakhmanov,[106] K. E. Ramirez,[106] A. Ramos-Buades,[104] Javed Rana,[18] P. Rapagnani,[98,34] V. Raymond,[35] M. Razzano,[21,22] J. Read,[28] T. Regimbau,[65,7] L. Rei,[60] S. Reid,[26] D. H. Reitze,[1,48] W. Ren,[11] F. Ricci,[98,34] P. M. Ricker,[11] K. Riles,[122] M. Rizzo,[58] N. A. Robertson,[1,44] R. Robie,[44] F. Robinet,[27] T. Robson,[103] A. Rocchi,[32] L. Rolland,[7] J. G. Rollins,[1] V. J. Roma,[69] R. Romano,[3,4] C. L. Romel,[45] J. H. Romie,[6] D. Rosińska,[155,54] M. P. Ross,[156] S. Rowan,[44] A. Rüdiger,[9,10] P. Ruggi,[30] G. Rutins,[157] K. Ryan,[45] S. Sachdev,[1] T. Sadecki,[45] M. Sakellariadou,[158] L. Salconi,[30] M. Saleem,[118] F. Salemi,[9] A. Samajdar,[148,13] L. Sammut,[5] L. M. Sampson,[90] E. J. Sanchez,[1] L. E. Sanchez,[1] N. Sanchis-Gual,[23] V. Sandberg,[45] J. R. Sanders,[42] N. Sarin,[5] B. Sassolas,[25] B. S. Sathyaprakash,[87,35] P. R. Saulson,[42] O. Sauter,[122] R. L. Savage,[45] A. Sawadsky,[33] P. Schale,[69] M. Scheel,[46] J. Scheuer,[90] P. Schmidt,[64] R. Schnabel,[33] R. M. S. Schofield,[69] A. Schönbeck,[33] E. Schreiber,[9,10] D. Schuette,[9,10] B. W. Schulte,[9,10] B. F. Schutz,[35,9] S. G. Schwalbe,[36] J. Scott,[44] S. M. Scott,[24] E. Seidel,[11] D. Sellers,[6] A. S. Sengupta,[159] D. Sentenac,[30] V. Sequino,[31,32,16] A. Sergeev,[128] Y. Setyawati,[9] D. A. Shaddock,[24] T. J. Shaffer,[45] A. A. Shah,[138] M. S. Shahriar,[90] M. B. Shaner,[110] L. Shao,[37] B. Shapiro,[49] P. Shawhan,[75] H. Shen,[11] D. H. Shoemaker,[14] D. M. Shoemaker,[76] K. Siellez,[76] X. Siemens,[20] M. Sieniawska,[54] D. Sigg,[45] A. D. Silva,[15] L. P. Singer,[79] A. Singh,[9,10] A. Singhal,[16,34] A. M. Sintes,[104] B. J. J. Slagmolen,[24] T. J. Slaven-Blair,[63] B. Smith,[6] J. R. Smith,[28] R. J. E. Smith,[5] S. Somala,[160] E. J. Son,[131] B. Sorazu,[44] F. Sorrentino,[60] T. Souradeep,[18] A. P. Spencer,[44] A. K. Srivastava,[108] K. Staats,[36] M. Steinke,[9,10]

J. Steinlechner,[33,44] S. Steinlechner,[33] D. Steinmeyer,[9,10] B. Steltner,[9,10] S. P. Stevenson,[154] D. Stocks,[49] R. Stone,[106] D. J. Stops,[59] K. A. Strain,[44] G. Stratta,[71,72] S. E. Strigin,[62] A. Strunk,[45] R. Sturani,[161] A. L. Stuver,[162] T. Z. Summerscales,[163] L. Sun,[97] S. Sunil,[108] J. Suresh,[18] P. J. Sutton,[35] B. L. Swinkels,[13] M. J. Szczepańczyk,[36] M. Tacca,[13] S. C. Tait,[44] C. Talbot,[5] D. Talukder,[69] D. B. Tanner,[48] M. Tápai,[119] A. Taracchini,[37] J. D. Tasson,[93] J. A. Taylor,[138] R. Taylor,[1] S. V. Tewari,[152] T. Theeg,[9,10] F. Thies,[9,10] E. G. Thomas,[59] M. Thomas,[6] P. Thomas,[45] K. A. Thorne,[6] E. Thrane,[5] S. Tiwari,[16,96] V. Tiwari,[35] K. V. Tokmakov,[26] K. Toland,[44] M. Tonelli,[21,22] Z. Tornasi,[44] A. Torres-Forné,[23] C. I. Torrie,[1] D. Töyrä,[59] F. Travasso,[30,41] G. Traylor,[6] J. Trinastic,[48] M. C. Tringali,[111,96] L. Trozzo,[164,22] K. W. Tsang,[13] M. Tse,[14] R. Tso,[46] D. Tsuna,[81] L. Tsukada,[81] D. Tuyenbayev,[106] K. Ueno,[20] D. Ugolini,[165] A. L. Urban,[1] S. A. Usman,[35] H. Vahlbruch,[9,10] G. Vajente,[1] G. Valdes,[2] N. van Bakel,[13] M. van Beuzekom,[13] J. F. J. van den Brand,[74,13] C. Van Den Broeck,[13,166] D. C. Vander-Hyde,[42] L. van der Schaaf,[13] J. V. van Heijningen,[13] A. A. van Veggel,[44] M. Vardaro,[51,52] V. Varma,[46] S. Vass,[1] M. Vasúth,[47] A. Vecchio,[59] G. Vedovato,[52] J. Veitch,[44] P. J. Veitch,[55] K. Venkateswara,[156] G. Venugopalan,[1] D. Verkindt,[7] F. Vetrano,[71,72] A. Viceré,[71,72] A. D. Viets,[20] S. Vinciguerra,[59] D. J. Vine,[157] J.-Y. Vinet,[65] S. Vitale,[14] T. Vo,[42] H. Vocca,[40,41] C. Vorvick,[45] S. P. Vyatchanin,[62] A. R. Wade,[1] L. E. Wade,[84] M. Wade,[84] R. Walet,[13] M. Walker,[28] L. Wallace,[1] S. Walsh,[20,9] G. Wang,[16,22] H. Wang,[59] J. Z. Wang,[122] W. H. Wang,[106] Y. F. Wang,[94] R. L. Ward,[24] J. Warner,[45] M. Was,[7] J. Watchi,[99] B. Weaver,[45] L.-W. Wei,[9,10] M. Weinert,[9,10] A. J. Weinstein,[1] R. Weiss,[14] F. Wellmann,[9,10] L. Wen,[63] E. K. Wessel,[11] P. Wessels,[9,10] J. Westerweck,[9] K. Wette,[24] J. T. Whelan,[58] B. F. Whiting,[48] C. Whittle,[14] D. Wilken,[9,10] D. Williams,[44] R. D. Williams,[1] A. R. Williamson,[58,64] J. L. Willis,[1,123] B. Willke,[9,10] M. H. Wimmer,[9,10] W. Winkler,[9,10] C. C. Wipf,[1] H. Wittel,[9,10] G. Woan,[44] J. Woehler,[9,10] J. K. Wofford,[58] W. K. Wong,[94] J. Worden,[45] J. L. Wright,[44] D. S. Wu,[9,10] D. M. Wysocki,[58] S. Xiao,[1] W. Yam,[14] H. Yamamoto,[1] C. C. Yancey,[75] L. Yang,[167] M. J. Yap,[24] M. Yazback,[48] Hang Yu,[14] Haocun Yu,[14] M. Yvert,[7] A. Zadrożny,[133] M. Zanolin,[36] T. Zelenova,[30] J.-P. Zendri,[52] M. Zevin,[90] J. Zhang,[63] L. Zhang,[1] M. Zhang,[143] T. Zhang,[44] Y.-H. Zhang,[9,10] C. Zhao,[63] M. Zhou,[90] Z. Zhou,[90] S. J. Zhu,[9,10] X. J. Zhu,[5] A. B. Zimmerman,[114] M. E. Zucker,[1,14] and J. Zweizig[1]

The LIGO Scientific Collaboration and the Virgo Collaboration

[1]*LIGO, California Institute of Technology, Pasadena, CA 91125, USA*

[2]*Louisiana State University, Baton Rouge, LA 70803, USA*

[3]*Università di Salerno, Fisciano, I-84084 Salerno, Italy*

[4]*INFN, Sezione di Napoli, Complesso Universitario di Monte S.Angelo, I-80126 Napoli, Italy*

[5]*OzGrav, School of Physics & Astronomy, Monash University, Clayton 3800, Victoria, Australia*

[6]*LIGO Livingston Observatory, Livingston, LA 70754, USA*

[7]*Laboratoire d'Annecy de Physique des Particules (LAPP), Univ. Grenoble Alpes, Université Savoie Mont Blanc, CNRS/IN2P3, F-74941 Annecy, France*

[8]*University of Sannio at Benevento, I-82100 Benevento, Italy and INFN, Sezione di Napoli, I-80100 Napoli, Italy*

[9]*Max Planck Institute for Gravitational Physics (Albert Einstein Institute), D-30167 Hannover, Germany*

[10]*Leibniz Universität Hannover, D-30167 Hannover, Germany*

[11]*NCSA, University of Illinois at Urbana-Champaign, Urbana, IL 61801, USA*

[12]*University of Cambridge, Cambridge CB2 1TN, United Kingdom*

[13]*Nikhef, Science Park 105, 1098 XG Amsterdam, The Netherlands*

[14]*LIGO, Massachusetts Institute of Technology, Cambridge, MA 02139, USA*

[15]*Instituto Nacional de Pesquisas Espaciais, 12227-010 São José dos Campos, São Paulo, Brazil*

[16]*Gran Sasso Science Institute (GSSI), I-67100 L'Aquila, Italy*

[17]*INFN, Laboratori Nazionali del Gran Sasso, I-67100 Assergi, Italy*

[18]*Inter-University Centre for Astronomy and Astrophysics, Pune 411007, India*

[19]*International Centre for Theoretical Sciences, Tata Institute of Fundamental Research, Bengaluru 560089, India*

[20]*University of Wisconsin-Milwaukee, Milwaukee, WI 53201, USA*

[21]*Università di Pisa, I-56127 Pisa, Italy*

[22]*INFN, Sezione di Pisa, I-56127 Pisa, Italy*

[23]*Departamento de Astronomía y Astrofísica, Universitat de València, E-46100 Burjassot, València, Spain*

[24]*OzGrav, Australian National University, Canberra, Australian Capital Territory 0200, Australia*

[25]*Laboratoire des Matériaux Avancés (LMA), CNRS/IN2P3, F-69622 Villeurbanne, France*

[26]*SUPA, University of Strathclyde, Glasgow G1 1XQ, United Kingdom*

[27]*LAL, Univ. Paris-Sud, CNRS/IN2P3, Université Paris-Saclay, F-91898 Orsay, France*

[28]*California State University Fullerton, Fullerton, CA 92831, USA*

[29]*APC, AstroParticule et Cosmologie, Université Paris Diderot, CNRS/IN2P3, CEA/Irfu, Observatoire de Paris, Sorbonne Paris Cité, F-75205 Paris Cedex 13, France*

[30]*European Gravitational Observatory (EGO), I-56021 Cascina, Pisa, Italy*

[31]*Università di Roma Tor Vergata, I-00133 Roma, Italy*

[32]*INFN, Sezione di Roma Tor Vergata, I-00133 Roma, Italy*

[33]*Universität Hamburg, D-22761 Hamburg, Germany*

[34]*INFN, Sezione di Roma, I-00185 Roma, Italy*

[35]*Cardiff University, Cardiff CF24 3AA, United Kingdom*
[36]*Embry-Riddle Aeronautical University, Prescott, AZ 86301, USA*
[37]*Max Planck Institute for Gravitational Physics (Albert Einstein Institute), D-14476 Potsdam-Golm, Germany*
[38]*Korea Institute of Science and Technology Information, Daejeon 34141, Korea*
[39]*West Virginia University, Morgantown, WV 26506, USA*
[40]*Università di Perugia, I-06123 Perugia, Italy*
[41]*INFN, Sezione di Perugia, I-06123 Perugia, Italy*
[42]*Syracuse University, Syracuse, NY 13244, USA*
[43]*University of Minnesota, Minneapolis, MN 55455, USA*
[44]*SUPA, University of Glasgow, Glasgow G12 8QQ, United Kingdom*
[45]*LIGO Hanford Observatory, Richland, WA 99352, USA*
[46]*Caltech CaRT, Pasadena, CA 91125, USA*
[47]*Wigner RCP, RMKI, H-1121 Budapest, Konkoly Thege Miklós út 29-33, Hungary*
[48]*University of Florida, Gainesville, FL 32611, USA*
[49]*Stanford University, Stanford, CA 94305, USA*
[50]*Università di Camerino, Dipartimento di Fisica, I-62032 Camerino, Italy*
[51]*Università di Padova, Dipartimento di Fisica e Astronomia, I-35131 Padova, Italy*
[52]*INFN, Sezione di Padova, I-35131 Padova, Italy*
[53]*MTA-ELTE Astrophysics Research Group, Institute of Physics, Eötvös University, Budapest 1117, Hungary*
[54]*Nicolaus Copernicus Astronomical Center, Polish Academy of Sciences, 00-716, Warsaw, Poland*
[55]*OzGrav, University of Adelaide, Adelaide, South Australia 5005, Australia*
[56]*Dipartimento di Scienze Matematiche, Fisiche e Informatiche, Università di Parma, I-43124 Parma, Italy*
[57]*INFN, Sezione di Milano Bicocca, Gruppo Collegato di Parma, I-43124 Parma, Italy*
[58]*Rochester Institute of Technology, Rochester, NY 14623, USA*
[59]*University of Birmingham, Birmingham B15 2TT, United Kingdom*
[60]*INFN, Sezione di Genova, I-16146 Genova, Italy*
[61]*RRCAT, Indore, Madhya Pradesh 452013, India*
[62]*Faculty of Physics, Lomonosov Moscow State University, Moscow 119991, Russia*
[63]*OzGrav, University of Western Australia, Crawley, Western Australia 6009, Australia*
[64]*Department of Astrophysics/IMAPP, Radboud University Nijmegen, P.O. Box 9010, 6500 GL Nijmegen, The Netherlands*
[65]*Artemis, Université Côte d'Azur, Observatoire Côte d'Azur, CNRS, CS 34229, F-06304 Nice Cedex 4, France*
[66]*Physik-Institut, University of Zurich, Winterthurerstrasse 190, 8057 Zurich, Switzerland*
[67]*Univ Rennes, CNRS, Institut FOTON - UMR6082, F-3500 Rennes, France*
[68]*Washington State University, Pullman, WA 99164, USA*
[69]*University of Oregon, Eugene, OR 97403, USA*
[70]*Laboratoire Kastler Brossel, Sorbonne Université, CNRS, ENS-Université PSL, Collège de France, F-75005 Paris, France*
[71]*Università degli Studi di Urbino 'Carlo Bo,' I-61029 Urbino, Italy*
[72]*INFN, Sezione di Firenze, I-50019 Sesto Fiorentino, Firenze, Italy*
[73]*Astronomical Observatory Warsaw University, 00-478 Warsaw, Poland*
[74]*VU University Amsterdam, 1081 HV Amsterdam, The Netherlands*
[75]*University of Maryland, College Park, MD 20742, USA*
[76]*School of Physics, Georgia Institute of Technology, Atlanta, GA 30332, USA*
[77]*Université Claude Bernard Lyon 1, F-69622 Villeurbanne, France*
[78]*Università di Napoli 'Federico II,' Complesso Universitario di Monte S.Angelo, I-80126 Napoli, Italy*
[79]*NASA Goddard Space Flight Center, Greenbelt, MD 20771, USA*
[80]*Dipartimento di Fisica, Università degli Studi di Genova, I-16146 Genova, Italy*
[81]*RESCEU, University of Tokyo, Tokyo, 113-0033, Japan.*
[82]*Tsinghua University, Beijing 100084, China*
[83]*Texas Tech University, Lubbock, TX 79409, USA*
[84]*Kenyon College, Gambier, OH 43022, USA*
[85]*The University of Mississippi, University, MS 38677, USA*
[86]*Museo Storico della Fisica e Centro Studi e Ricerche "Enrico Fermi", I-00184 Roma, Italyrico Fermi, I-00184 Roma, Italy*
[87]*The Pennsylvania State University, University Park, PA 16802, USA*
[88]*National Tsing Hua University, Hsinchu City, 30013 Taiwan, Republic of China*
[89]*Charles Sturt University, Wagga Wagga, New South Wales 2678, Australia*
[90]*Center for Interdisciplinary Exploration & Research in Astrophysics (CIERA), Northwestern University, Evanston, IL 60208, USA*
[91]*University of Chicago, Chicago, IL 60637, USA*

[92]*Pusan National University, Busan 46241, Korea*
[93]*Carleton College, Northfield, MN 55057, USA*
[94]*The Chinese University of Hong Kong, Shatin, NT, Hong Kong*
[95]*INAF, Osservatorio Astronomico di Padova, I-35122 Padova, Italy*
[96]*INFN, Trento Institute for Fundamental Physics and Applications, I-38123 Povo, Trento, Italy*
[97]*OzGrav, University of Melbourne, Parkville, Victoria 3010, Australia*
[98]*Università di Roma 'La Sapienza,' I-00185 Roma, Italy*
[99]*Université Libre de Bruxelles, Brussels 1050, Belgium*
[100]*Sonoma State University, Rohnert Park, CA 94928, USA*
[101]*Departamento de Matemáticas, Universitat de València, E-46100 Burjassot, València, Spain*
[102]*Columbia University, New York, NY 10027, USA*
[103]*Montana State University, Bozeman, MT 59717, USA*
[104]*Universitat de les Illes Balears, IAC3—IEEC, E-07122 Palma de Mallorca, Spain*
[105]*University of Rhode Island*
[106]*The University of Texas Rio Grande Valley, Brownsville, TX 78520, USA*
[107]*Bellevue College, Bellevue, WA 98007, USA*
[108]*Institute for Plasma Research, Bhat, Gandhinagar 382428, India*
[109]*The University of Sheffield, Sheffield S10 2TN, United Kingdom*
[110]*California State University, Los Angeles, 5151 State University Dr, Los Angeles, CA 90032, USA*
[111]*Università di Trento, Dipartimento di Fisica, I-38123 Povo, Trento, Italy*
[112]*Montclair State University, Montclair, NJ 07043, USA*
[113]*National Astronomical Observatory of Japan, 2-21-1 Osawa, Mitaka, Tokyo 181-8588, Japan*
[114]*Canadian Institute for Theoretical Astrophysics, University of Toronto, Toronto, Ontario M5S 3H8, Canada*
[115]*Observatori Astronòmic, Universitat de València, E-46980 Paterna, València, Spain*
[116]*School of Mathematics, University of Edinburgh, Edinburgh EH9 3FD, United Kingdom*
[117]*University and Institute of Advanced Research, Koba Institutional Area, Gandhinagar Gujarat 382007, India*
[118]*Indian Institute of Technology Bombay*
[119]*University of Szeged, Dóm tér 9, Szeged 6720, Hungary*
[120]*Tata Institute of Fundamental Research, Mumbai 400005, India*
[121]*INAF, Osservatorio Astronomico di Capodimonte, I-80131, Napoli, Italy*
[122]*University of Michigan, Ann Arbor, MI 48109, USA*
[123]*Abilene Christian University, Abilene, TX 79699, USA*
[124]*American University, Washington, D.C. 20016, USA*
[125]*University of Białystok, 15-424 Białystok, Poland*
[126]*University of Southampton, Southampton SO17 1BJ, United Kingdom*
[127]*University of Washington Bothell, 18115 Campus Way NE, Bothell, WA 98011, USA*
[128]*Institute of Applied Physics, Nizhny Novgorod, 603950, Russia*
[129]*Korea Astronomy and Space Science Institute, Daejeon 34055, Korea*
[130]*Inje University Gimhae, South Gyeongsang 50834, Korea*
[131]*National Institute for Mathematical Sciences, Daejeon 34047, Korea*
[132]*Ulsan National Institute of Science and Technology*
[133]*NCBJ, 05-400 Świerk-Otwock, Poland*
[134]*Institute of Mathematics, Polish Academy of Sciences, 00656 Warsaw, Poland*
[135]*Cornell Universtiy*
[136]*Hillsdale College, Hillsdale, MI 49242, USA*
[137]*Hanyang University, Seoul 04763, Korea*
[138]*NASA Marshall Space Flight Center, Huntsville, AL 35811, USA*
[139]*Dipartimento di Fisica, Università degli Studi Roma Tre, I-00154 Roma, Italy*
[140]*INFN, Sezione di Roma Tre, I-00154 Roma, Italy*
[141]*ESPCI, CNRS, F-75005 Paris, France*
[142]*Southern University and A&M College, Baton Rouge, LA 70813, USA*
[143]*College of William and Mary, Williamsburg, VA 23187, USA*
[144]*Centre Scientifique de Monaco, 8 quai Antoine Ier, MC-98000, Monaco*
[145]*Indian Institute of Technology Madras, Chennai 600036, India*
[146]*INFN Sezione di Torino, Via P. Giuria 1, I-10125 Torino, Italy*
[147]*Institut des Hautes Etudes Scientifiques, F-91440 Bures-sur-Yvette, France*
[148]*IISER-Kolkata, Mohanpur, West Bengal 741252, India*

[149] *Whitman College, 345 Boyer Avenue, Walla Walla, WA 99362 USA*
[150] *Scuola Normale Superiore, Piazza dei Cavalieri 7, I-56126 Pisa, Italy*
[151] *Université de Lyon, F-69361 Lyon, France*
[152] *Hobart and William Smith Colleges, Geneva, NY 14456, USA*
[153] *Università degli Studi di Firenze, I-50121 Firenze, Italy*
[154] *OzGrav, Swinburne University of Technology, Hawthorn VIC 3122, Australia*
[155] *Janusz Gil Institute of Astronomy, University of Zielona Góra, 65-265 Zielona Góra, Poland*
[156] *University of Washington, Seattle, WA 98195, USA*
[157] *SUPA, University of the West of Scotland, Paisley PA1 2BE, United Kingdom*
[158] *King's College London, University of London, London WC2R 2LS, United Kingdom*
[159] *Indian Institute of Technology, Gandhinagar Ahmedabad Gujarat 382424, India*
[160] *Indian Institute of Technology Hyderabad, Sangareddy, Khandi, Telangana 502285, India*
[161] *International Institute of Physics, Universidade Federal do Rio Grande do Norte, Natal RN 59078-970, Brazil*
[162] *Villanova University, 800 Lancaster Ave, Villanova, PA 19085, USA*
[163] *Andrews University, Berrien Springs, MI 49104, USA*
[164] *Università di Siena, I-53100 Siena, Italy*
[165] *Trinity University, San Antonio, TX 78212, USA*
[166] *Van Swinderen Institute for Particle Physics and Gravity, University of Groningen, Nijenborgh 4, 9747 AG Groningen, The Netherlands*
[167] *Colorado State University, Fort Collins, CO 80523, USA*

* Deceased, February 2018.
† Deceased, November 2017.